
A Probabilistic Framework for Predicting Spatiotemporal Intensity and Variability of Outdoor Thermal Comfort

Shisheng Chen^{a, b}, Ruohan Xu^{b, *}, Nyuk Hien Wong^b, Shanshan Tong^b, Jiashuo Wang^c, Matthaïos Santamouris^c

a-School of Architecture and Urban-rural Planning, Fuzhou University, P.R. China 350108.

b-Department of the Built Environment, National University of Singapore, Singapore 117566.

c-School of Built Environment, University of New South Wales, Australia 2052.

*Corresponding author.

E-mail address: bdgxr@nus.edu.sg (R. Xu)

Abstract

Thermal conditions in the urban canopy exhibit stochastic variability driven by varied radiative fluxes and turbulent wind fields requiring probabilistic rather than deterministic prediction methods. This study presents a probabilistic framework for predicting the spatial and temporal intensity and variability of outdoor thermal comfort in tropical urban environments. The framework integrated ground measured meteorological data and remote sensing urban morphological data to calculate Physiological Equivalent Temperature (PET), and uses K-means, XGBoost and Monte Carlo simulations on PET's training and inference. The prediction model achieved strong predictive performance, with R^2 , RMSE, and SMAPE values of 0.93, 0.81 °C, and 1.34% for PET_{mean} , and 0.85, 0.38 °C, and 10.44% for PET_{std} , respectively. Case study showed clear spatial heterogeneity of outdoor thermal comfort. Locations with dense tree canopies and vegetated surfaces displayed the normalized percentage of acceptable thermal comfort (NATC) up to 65%, whereas built-up zones dominated by impervious surfaces, such as industrial estates and high-density residential areas, recorded NATC below 30%. Greenery was found to mitigate both the intensity of heat stress and its variability, producing a stable and comfortable microclimate. Daytime PET_{std} ranged from 4.0–4.5 °C in built-up areas to 1.5–2.0 °C in greenery-covered zones, while nighttime PET_{std} decreased to 2.2–2.4 °C and 1.2–1.4 °C, respectively. These findings emphasize the critical role of greenery in mitigating thermal variability and enhancing outdoor thermal comfort, while revealing the stochastic nature of thermal comfort across different urban morphologies.

Keywords: Outdoor Thermal Comfort; Physiological Equivalent Temperature; Heat Stress; Clustering; Regression; Probabilistic Prediction

Nomenclature

Symbol	Meaning
PET	Physiological equivalent temperature
QUEST	Quantitative urban environment simulation tool
GEE	Google earth engine
PCA	Principal component analysis
SC	Silhouette coefficient
DBI	Davies–bouldin index
CHI	Calinski–harabasz index
SMAPE	Symmetric mean absolute percentage error, %
RMSE	Root mean squared error, °C
R^2	Coefficient of determination
PET_{mean}	Mean of physiological equivalent temperature, °C
PET_{std}	Standard deviation of physiological equivalent temperature, °C
T_a	Dry-bulb air temperature, °C
T_{mrt}	Mean radiant temperature, °C
V_a	Air speed, m/s
RH	Relative humidity, %
NDVI	Normalized difference vegetation index
MNDWI	Modified normalized difference water index
NDBI	Normalized Difference Built-up Index
BSI	Bare soil index
α_{land}	Land surface albedo
ϵ_{land}	Land surface emissivity
NIR	Near-infrared reflectance
$SWIR$	Shortwave infrared reflectance
Pv	Fractional vegetation cover

ϵ_s	Soil emissivity
ϵ_v	Vegetation emissivity
NATC	Normalized percentage of acceptable thermal comfort, %
$N_{c,h}$	Number of observations belonging to acceptable thermal comfort at hour h
N	Total number of observations over at hour h
c	Set of acceptable heat stress categories including slight cold stress, no heat stress, slight heat stress
$Rain_{tot}$	Total rainfall, mm
$Wind_{avg}$	Wind speed, m/s
$Solar_{tot}$	Total global horizontal solar irradiance, W/m^2
$Solar_{max}$	Maximum global horizontal solar irradiance, W/m^2
$Solar_{avg}$	Mean global horizontal solar irradiance, W/m^2
T_{avg}	Average air temperature, $^{\circ}C$
T_{max}	Maximum air temperature, $^{\circ}C$
T_{min}	Minimum air temperature, $^{\circ}C$
$T_{air_{ref}}$	Reference dry-bulb air temperature, $^{\circ}C$
$Solar_{ref}$	Reference global horizontal solar irradiance, W/m^2
$V_{a_{ref}}$	Reference wind speed, m/s

1. Introduction

1.1 Outdoor Thermal Comfort Assessment

Assessing outdoor thermal comfort is essential for enhancing urban heat resilience and can be approached through objective assessments and subjective questionnaires. Objective assessments typically rely on either microclimate simulations or onsite measurements. Simulations such as Computational Fluid Dynamics (CFD) are suitable for large-scale evaluations but require extensive computational resources and validation. In contrast, onsite measurements offer higher spatial accuracy but are limited by the number of sampling points. Both approaches face challenges in accuracy due to the need to interpolate data across unmeasured areas, which introduces potential uncertainty into thermal comfort assessments.

Several integrative thermal indices derived from the human energy balance such as physiological equivalent temperature (PET) (Höppe, 1999), universal thermal climate index (UTCI) (Bröde et al., 2012), and outdoor standard effective temperature (OUT_SET*) (Spagnolo and De Dear, 2003) have been developed to quantify human thermal comfort.

The Physiological Equivalent Temperature (PET) is an important index for evaluating human thermal comfort in outdoor environments, particularly in the context of urban heat islands and occupational health and safety (Farhadi et al., 2019; Fiorillo et al., 2023; Hwang et al., 2023). PET is derived from the Munich Energy Balance Model for Individuals (MEMI) by Hoppe and represents the air temperature at which the human energy budget is maintained under specific conditions of skin temperature and core temperature (Höppe, 1999). PET enables a comparison of complex thermal conditions outside with one's own experience indoors, allowing for a more intuitive understanding of thermal comfort or discomfort. Walther and Goestchel propose a correction to the PET calculation defined by Hoppe and compare the corrected model with the original method, highlighting errors in calculation routine and vapor diffusion model (Walther and Goestchel, 2018). For example, the original PET model uses a simplified approach to solve the equation system, while the corrected model provides a more rigorous solution, leading to more accurate assessments of thermal comfort. In addition, the vapor diffusion model of the original PET model is not dependent on the clothing insulation, an issue addressed by the corrected model by aligning it with state-of-the-art vapor transport models. The corrected PET model of Walther and Goestchel is later adopted by the pythermalcomfort package using dry-bulb air temperature (T_a), mean radiant temperature (T_{mrt}), air speed (V_a), relative humidity (RH), metabolic rate and clothing insulation as input parameters to calculate PET (Tartarini and Schiavon, 2020).

Universal Thermal Climate Index (UTCI) was developed by the International Society of Biometeorology (ISB) following the need for a thermal comfort model suitable for outdoor applications (Błażejczyk et al., 2010). UTCI aims to assess outdoor thermal conditions in the major fields of human biometeorology in terms of a one-dimensional quantity reflecting the human physiological reaction to the multidimensionally defined actual outdoor thermal environment, including environmental temperature, wind speed, humidity, long-wave and short-wave radiant heat fluxes (Bröde et al., 2012). The human reaction was simulated by the UTCI-Fiala multi-node model of human thermoregulation, which was integrated with an adaptive clothing model (Fiala et al., 2012).

The outdoor standard effective temperature index is an outdoor version of the widely used indoor comfort index called the standard effective temperature (SET*), incorporating air and mean radiant temperatures, relative humidity, air velocity, clothing insulation and activity level (Spagnolo and De Dear, 2003). SET* is defined as the temperature of hypothetical isothermal reference environment ($T_{mrt} = T_a$; RH= 50%; $V_a < 0.15\text{m/s}$) such that a person in the reference environment wearing 0.6 clo and standing still (1.2 met) has the same mean skin temperature and skin wettedness as the person in the actual complex environment. In the outdoor version (OUT_SET*), the assumption that $T_{mrt} = T_a$ is relaxed, and the actual mean radiant temperature is calculated using a human thermoregulatory model

developed by Jendritzky and Staiger (Spagnolo and De Dear, 2003). Compared with PET and UTCI, OUT_SET* is less widely used and its predictive capabilities still need to be tested.

At neighbourhood scales, urban land cover and morphology systematically modulate the radiative and convective exchanges that shape local microclimate and outdoor thermal comfort. Recent studies increasingly use remotely sensed indicators as standard proxies for these controls. For example, vegetation indices capture shading and evapotranspiration cooling (Carlson, 2019; Chen et al., 2006; Dobrovolný and Krahula, 2015; Imran et al., 2021; Jamei et al., 2022; Jia and Wang, 2020), and water-related indices reflect advection and the thermal inertia of open water (Chen et al., 2006; Imran et al., 2021; Jia and Wang, 2020; Xu, 2006). In addition, built-up and bare-soil metrics indicate imperviousness and surface moisture status (Chen et al., 2020, 2020, 2006; Guo et al., 2022; Imran et al., 2021; Jamei et al., 2022; Jia and Wang, 2020; Zha et al., 2003), and broadband albedo and surface emissivity parameterize short-wave reflection and long-wave exchange (Chen et al., 2023; He et al., 2025; Musco et al., 2016; Tabatabaei and Fayaz, 2023; Vuckovic et al., 2016). Consistent empirical evidence shows that higher fractions of vegetation and water are associated with reduced surface thermal loads and improved outdoor conditions, whereas greater imperviousness and exposed soils intensify heat exposure (Chatterjee and Majumdar, 2022; Imran et al., 2021; Jamei et al., 2022; Kumar Gavsker, 2023). These findings motivate the use of satellite-derived morphology as explanatory covariates for spatially explicit thermal comfort assessments when paired with ground-level meteorology.

1.2 The Sampling Framework and Analysis of Outdoor Thermal Comfort

PET assessment procedures involve a sequence of microclimate monitoring, PET calculation, heat stress classification, and impact evaluation. Firstly, PET is derived from high-resolution microclimate measurements, including 1-min logging of T_a , RH, V_a , and T_{globe} at various heights such as pedestrian level, mid-level, and rooftop (Miao et al., 2023). Similar data were collected through 1-min observations at twelve factory sites during three clear winter days in Haining (He et al., 2023), 1-min to 30-min mobile scans at 23 street canyon points in Harbin from July 2020 to January 2021 (Sun et al., 2022), and 1-min to 5-min logging within two sunken squares during two seven-day surveys in winter and summer in Shenzhen (Zhao et al., 2023).

PET is then computed using tools like RayMan (He et al., 2023; Miao et al., 2023) or ENVI-met BIO-met, incorporating measured environmental parameters along with clothing insulation and metabolic rates derived from questionnaire responses (Tabatabaei and Fayaz, 2023). Thermal sensation votes are then correlated with PET values to calculate the neutral PET ranges or 80% acceptability ranges. For instance, the correlation between mean thermal sensation votes with PET binned at 1 °C intervals yields neutral PET ranges of 14.3 °C in winter (He et al., 2023), 29 °C in summer (Zhao et al., 2023), and 14.5–22.8 °C across four seasons (Sun et al., 2022), as well as 80% acceptability ranges of 7.9–27.3 °C at cold region (Sun et al., 2022) and 10.7–17.8 °C in humid subtropical climate (He et al., 2023). In addition, regression analysis is performed to quantify the influence of urban design factors on PET, such as façade material properties (e.g., solar reflectance, emissivity) (Lopez-Cabeza et al., 2022; Tabatabaei and Fayaz, 2023), and street geometry variables (e.g., sky view factor, aspect ratio) (Muniz-Gäl et al., 2020; Sun et al., 2022). These field measurements are frequently supplemented by simulations. For instance, hourly TMY3-driven Ladybug modelling was conducted for 18 shading configurations over three summer months in Taichung to validate the PET condition (Ou and Lin, 2023). The impact of twenty façade materials on PET was evaluated through 24-hour ENVI-met BIO-met running on summer and winter days in Shiraz (Tabatabaei and Fayaz, 2023).

Translating morphology and meteorology into site-specific and hour-by-hour comfort estimates benefits from data-driven models that can learn nonlinear interactions while remaining interpretable (Lamberti et al., 2023). Predictive models coupled with machine learning interpretable techniques such as SHAP analysis meet this need as the models can estimate not only the expected value of PET but

also its dispersion (e.g., standard deviation), and SHAP provides an additive and physically interpretable attribution of each predictor's contribution (Li et al., 2025). Together, these tools enable probabilistic and explainable mapping of outdoor thermal comfort.

1.3 Research Gap and Objectives

Microclimatic conditions within the urban canopy are governed by varied radiation fluxes and complex wind fields leading to significant spatiotemporal variability in thermal comfort perception. This stochastic variability arises from the interactions between surface-atmosphere energy exchange, turbulence, and localized shading effects, and therefore cannot be reliably represented by deterministic methods. Instead, probabilistic modelling tools are needed to capture the likelihood distribution of thermal comfort outcomes. Although PET is frequently used in thermal comfort assessments, most studies rely on deterministic approaches employing fixed values or averaged environmental conditions for PET calculation, which neglects the inherent variability and uncertainty in meteorological and human-related parameters. This limitation is partly due to the short measurement period whereas temperatures, humidity and wind speed can fluctuate widely even in the same hot weather conditions when observed over longer periods. To overcome this, it is important to incorporate variability statistics (e.g., standard deviation) and stochastic modelling (e.g., Monte Carlo simulation) into thermal comfort assessments. In this study, a probabilistic framework for outdoor thermal comfort modelling has been developed under clear and hot weather conditions. The framework not only predicts the expected mean PET but also quantifies its uncertainty through the distribution of PET values. The objectives of this study were to: (a) evaluate spatial and temporal patterns of intensity and variability of PET across an urban region; (b) identify key urban morphological features influencing both the mean and standard deviation of PET; (c) explain the morphological drivers of thermal hotspots to support targeted heat mitigation strategies.

The remaining structure of paper is organized as follows. The research design is described in Section 2, including data collection of meteorological data, remote sensing data, calculation of outdoor thermal comfort, and probabilistic prediction framework. Section 3 presents the results of spatial and temporal spatial and temporal heterogeneity of PET across sampled locations and prediction performance of probabilistic models. Section 4 and Section 5 discuss and concludes the potential and limitation of probabilistic models and key drivers behind the intensity and variability of outdoor thermal comfort.

2. Methodology

2.1 Research Design

The research framework (Figure 1) integrates ground-measured meteorological observations with multispectral remote sensing data to characterize the spatiotemporal heterogeneity of urban thermal comfort. Following rigorous quality control, microclimatic data were employed to derive hourly PET values across sampled locations. K-means clustering was applied to classify reference meteorological data conditioned by radiation, temperature, and wind. XGBoost regression was applied to link PET with environmental and morphological predictors at unsampled locations. The Monte Carlo simulation based on trained models produced continuous spatial mapping of PET and NATC, providing high-resolution maps of heat exposure to support planning and policy assessment.

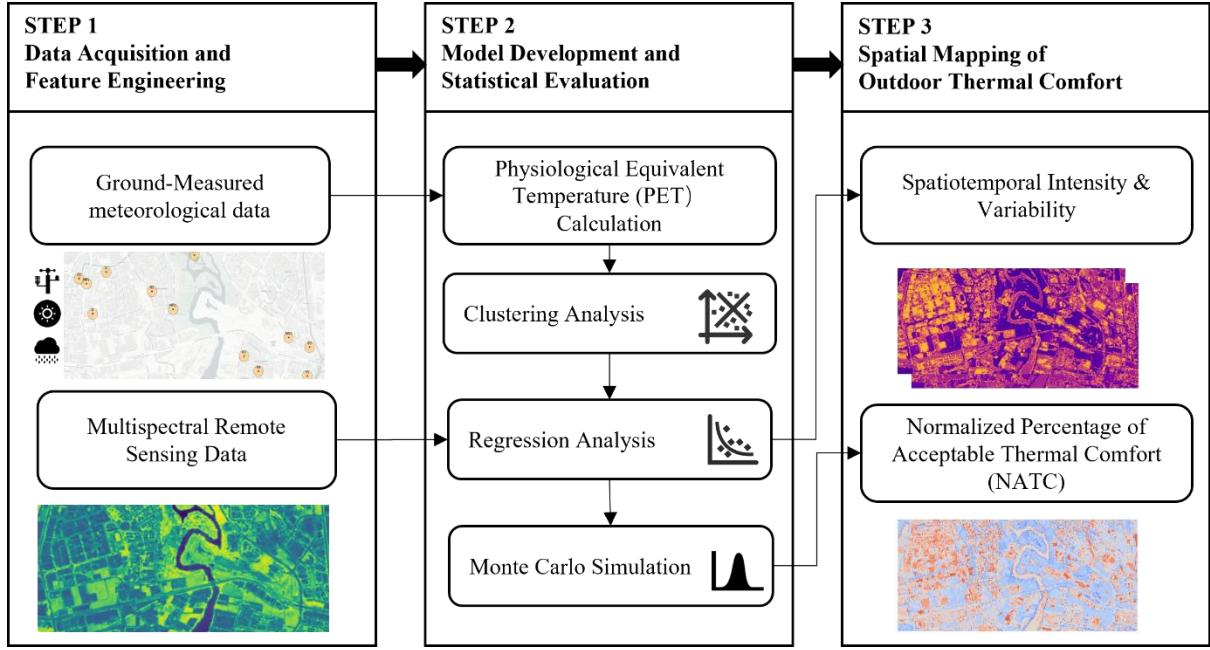


Figure 1: Probabilistic prediction framework for outdoor thermal comfort

2.2 Collection of Meteorological Data

This study demonstrated the prediction performance of proposed model using the ground-level microclimate data collected from Quantitative Urban Environment Simulation Tool (QUEST), a platform for analysing and testing the immediate microclimatic impact of development plans and assessing their long-term impacts under future climate change scenarios in Singapore (Lim et al., 2021). The QUEST data was collected in the eastern part of Singapore, recording meteorological data including T_{globe} , T_a , RH, and V_a at 5-minute interval from Feb 19th 2018 to Dec 8th 2018. The selected measurement points are shown in the OpenStreetMap (Figure 2) (Boeing, 2024). Points prefixed with R and B indicate measurement locations in residential areas and business areas, respectively. Points prefixed with I and P indicate measurement locations in industrial areas and parks, respectively. Points prefixed with MR represent major roads.

Table 1 illustrated the instruments used in this study. T_a and RH were measured using ONSET U23-001 HOBO PRO V2 INT TEMP/RH. V_a was measured using ONSET S-WSB & WDA -M003. T_{globe} was measured using ONSET UX100-014M T DATA LOGGER with grey ping pong and thermo-couple wire.

T_{mrt} was calculated from Equation (1) based on the calibrated mean convection coefficient using a 40 mm grey globe with an emissivity of 0.97 in Singapore (Tan et al., 2013). The calibrated T_{mrt} equation is only valid for $0 \text{ m/s} \leq V_a \leq 4 \text{ m/s}$ (Tan et al., 2013) used as the criterion for filtering out meteorological data.

$$T_{\text{mrt}} = [(T_{\text{globe}} + 273.15)^4 + \frac{3.42 \times 10^9 V_a^{0.119}}{\epsilon \times D^{0.4}} \times (T_{\text{globe}} - T_a)]^{0.25} - 273.15 \quad (1)$$

Where T_{globe} is the globe temperature ($^{\circ}\text{C}$); T_a is the air temperature ($^{\circ}\text{C}$); V_a is the wind speed (m/s); D is the globe diameter (mm); ϵ is the emissivity of globe.

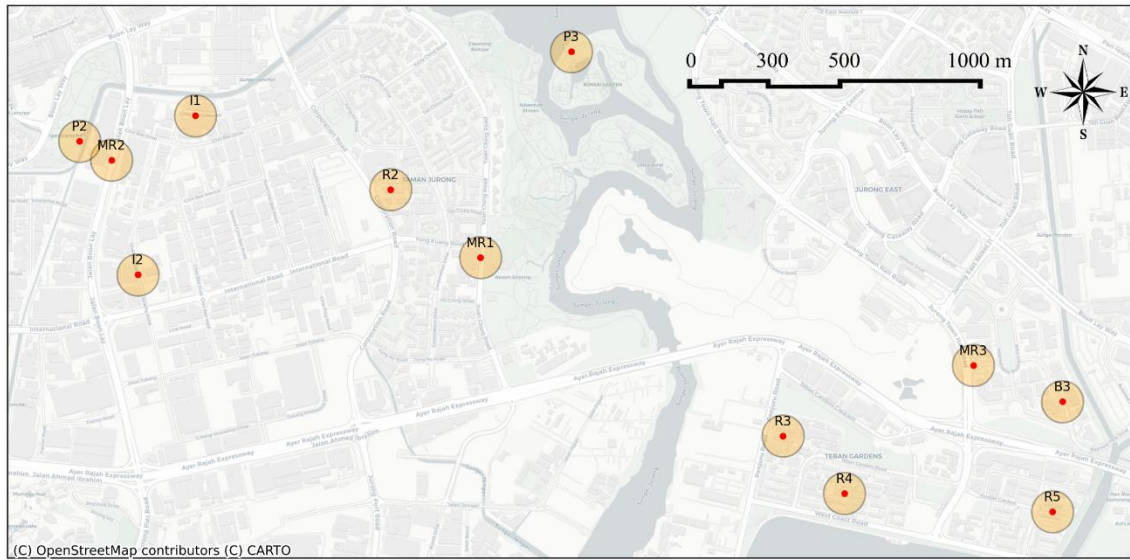


Figure 2: Locations of measurement points

Table 1: Specifications of instruments

Sensors	Variable(s)	Measurement range	Accuracy	Sampling rate
ONSET U23-001 HOBO PRO V2 INT TEMP/RH	T_a & RH	-40° to 70°C	±0.21°C	5-minute
		0-100%	±2.5%	
ONSET S-WSB	V_a	0 to 76 m/s	±1.1m/s	5-minute

ONSET UX100-014M T DATA LOGGER with grey ping pong and thermo-couple wire	T_{globe}	-20° to 70°C	±0.21°C	5-minute
--	--------------------	--------------	---------	----------

2.3 Collection of Multispectral Remote Sensing Data

To characterize the land surface conditions surrounding each sampling point, a group of remote sensing indices were derived using Sentinel-2 satellite multispectral data (surface reflectance imagery) processed via Google Earth Engine (GEE) (Gorelick et al., 2017). The imagery was filtered for cloud cover (<20%) within the study period (2018–2020) and spatially constrained to a specified buffer radius of 100m around each point. For each sampling point, several indices representing vegetation, water, and built-up area were calculated including the Normalized Difference Vegetation Index (*NDVI*), Modified Normalized Difference Water Index (*MNDWI*), Normalized Difference Built-up Index (*NDBI*), Bare Soil Index (*BSI*), land surface albedo (α_{land}), and land surface emissivity (ϵ_{land}) using corresponding Sentinel-2 satellite bands, as shown in Table 2. The surface reflectance imagery was used to extract mean values for each index within the buffer zone. These remotely sensed metrics were subsequently used as independent variables in the machine learning models for predicting outdoor thermal comfort conditions. The computed urban morphological values are shown in Figure 3.

Table 2: Selected Sentinel-2 satellite bands used in this study

Band	Central Wavelength (nm)	Resolution (m)	Band Number (Sentinel-2)
Blue	490	10	B2
Green	560	10	B3
Red	665	10	B4
NIR	842	10	B8
SWIR1	1610	20	B11
SWIR2	2190	20	B12

NDVI is based on the difference of reflectance in the near-infrared and red bands (Lillesand et al., 2015):

$$NDVI = \frac{NIR - Red}{NIR + Red} \quad (2)$$

where *NIR* is the near-infrared reflectance and *Red* is the red reflectance.

NDBI is referred to the difference of reflectance between TM Band 4 (0.76-0.9μm) and TM Band 5 (1.55-1.75μm) bands (Zha et al., 2003):

$$NDBI = \frac{SWIR1 - NIR}{SWIR1 + NIR} \quad (3)$$

where *SWIR1* is the shortwave infrared reflectance with a central wavelength of 1.61μm.

MNDWI is originally derived based on TM Band 5 (1.55-1.75μm) and TM Band 2 (Green) from Landsat 5 (Xu, 2006):-

$$MNDWI = \frac{Green - SWIR1}{Green + SWIR1} \quad (4)$$

where *Green* is the green reflectance.

BSI represents exposed soil surfaces and uncultivated areas and is formulated using Equation (Mzid et al., 2021; Rikimaru et al., 2002):

$$BSI = \frac{(SWIR1 + Red) - (NIR + Blue)}{(SWIR1 + Red) + (NIR + Blue)} \quad (5)$$

where *Blue* is the blue reflectance.

α_{land} is estimated as a weighted combination of visible, NIR, and shortwave infrared reflectance bands (Smith, 2010):

$$\alpha_{land} = \frac{0.356Blue + 0.130Red + 0.373NIR + 0.085SWIR1 + 0.072SWIR2 - 0.0018}{1.016} \quad (6)$$

where *SWIR2* corresponds to Sentinel-2 Band 12.

ϵ_{land} was estimated from NDVI based on fractional vegetation cover approach (Carlson, 2019; Sobrino et al., 2008, 2004):

$$Pv = \left(\frac{NDVI - 0.2}{0.5 - 0.2} \right)^2 \quad (7)$$

$$\epsilon_{land} = Pv \times \epsilon_v + (1 - Pv) \times \epsilon_s + 0.005 \quad (8)$$

Where *Pv* is the fractional vegetation cover; ϵ_v is the vegetation emissivity with field measured value of 0.985±0.007 (Sobrino et al., 2008; Valor and Caselles, 1996); ϵ_s is the soil emissivity with field measured value of 0.96±0.01 (Valor and Caselles, 1996).

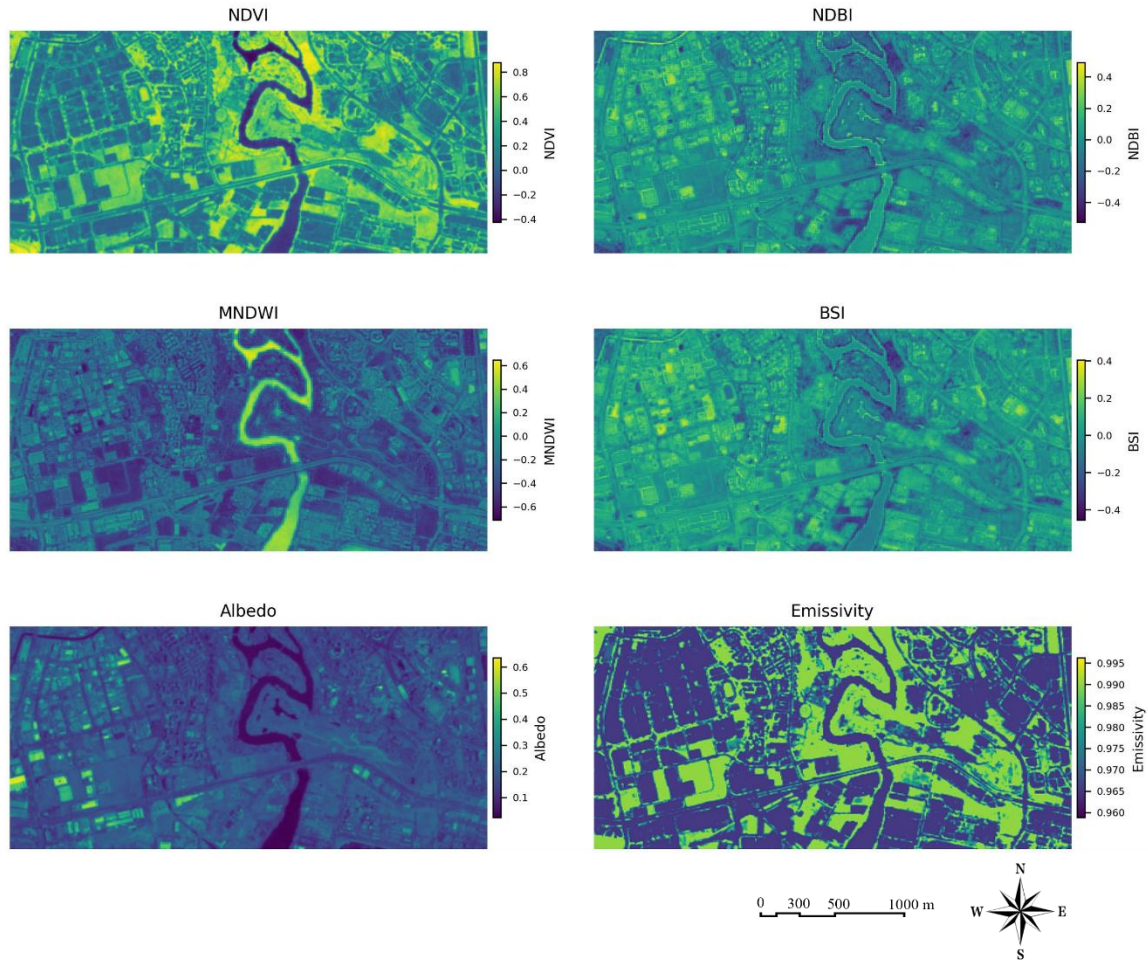


Figure 3: Urban morphological index extracted from satellite images

2.4 Calculation of Outdoor Thermal Comfort

Summer metabolic rate and clothing insulation levels were set to 2.0 met and 0.5 clo, respectively, in accordance with ASHRAE Standard 55 (ASHRAE, 2017), representing individuals walking at 0.9 m/s meanwhile wearing typical summer attire. PET calculation model was running through pythermalcomfort (Tartarini and Schiavon, 2020) with input features including T_a , T_{mrt} , V_a , and RH. Each simulated PET value was subsequently classified into heat stress levels based on thresholds (Figure 4) calibrated by Singapore's Building and Construction Authority based on thermal comfort perception studies involving local residents (Building and Construction Authority, 2021).

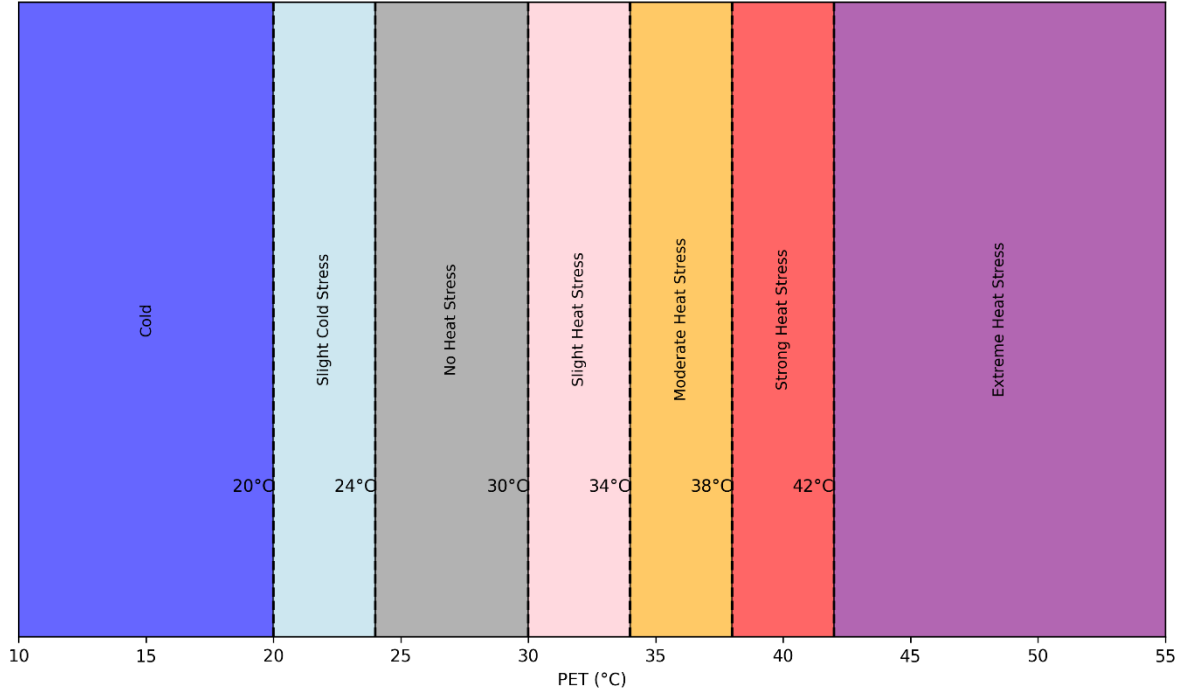


Figure 4: Heat stress level classification of PET used in Singapore

This study considered PET values below 34°C excluding moderate to extreme heat stress as acceptable thermal comfort suitable for outdoor activities. Normalized percentage of acceptable thermal comfort (NATC) is then formulated:

$$NATC(\%) = \frac{1}{24} \sum_{h=0}^{23} \left(\frac{N_{c,h}}{N} * 100\% \right) \quad (9)$$

Where $N_{c,h}$ is the number of observations belonging to acceptable thermal comfort at hour h ; N is the total number of observations over at hour h ; c is the set of acceptable heat stress categories (Slight Cold Stress, No Heat Stress, Slight Heat Stress).

2.5 Probabilistic Prediction Framework

2.5.1 Clustering of Reference Meteorological Data

The cluster analysis was initiated with reference meteorological data as inputs. These hourly data were aggregated into daily metrics consisting of total rainfall ($Rain_{tot}$), average wind speed ($Wind_{avg}$), total global horizontal solar irradiance ($Solar_{tot}$), maximum global horizontal solar irradiance ($Solar_{max}$), mean global horizontal solar irradiance ($Solar_{avg}$), air temperature (T_{avg}), maximum air temperature (T_{max}), and minimum air temperature (T_{min}).

The resulting daily data were then normalized to a 0–1 range before clustering. The K-means algorithm implemented using `sklearn.cluster.KMeans` (Arthur and Vassilvitskii, 2007; Pedregosa et al., 2011) was employed to group the samples by minimizing inertia. To enhance the clustering performance, Principal Component Analysis (PCA) was applied, projecting the original data into a lower-dimensional space. In this study, PCA was implemented using `sklearn.decomposition.PCA` (Pedregosa et al., 2011), with

the number of components set to 2 thereby reducing the dataset to a two-dimensional representation. Clustering was performed with the number of clusters ranging from 2 to 7.

Inertia measures the compactness of clusters by summing squared distances between each point and its cluster centroid:

$$Inertia = \sum_{j=1}^k \sum_{i=1}^n \min \|x_i^j - c_j\|^2 \quad (10)$$

Where k is the number of clusters, n is the number of samples, x_i^j is sample i in cluster j , c_j is centroid of cluster j . After running the clustering algorithm, each sample of meteorological data was labelled by a numerical value to indicate the classification of clusters (e.g. 0 for cluster 0). Lower inertia indicates more compact clusters.

In addition, this study also applied Silhouette Coefficient (SC), Davies–Bouldin Index (DBI), Calinski–Harabasz Index (CHI) from `sklearn.metrics` (Pedregosa et al., 2011) for clustering evaluation.

SC measures both intra-cluster distance and nearest-cluster distance. For each sample:

$$SC(i) = \frac{b(i) - a(i)}{\max(a(i) - b(i))} \quad (11)$$

Where a is the mean intra-cluster distance (the distance among samples of a cluster), b is the distance between the sample and the closest cluster to which the sample does not belong. The best value and the worst value are 1 and -1, respectively, and values close to 0 indicate overlapping clusters.

DBI quantifies average similarity between each cluster and its most similar one using intra-cluster scatter and between-cluster separation:

$$DBI = \frac{1}{k} \sum_{i=1}^k \max_{i \neq j} \frac{s_i + s_j}{d_{ij}} \quad (12)$$

Where s_i and s_j represents intra-cluster distances for clusters i and j , respectively; d_{ij} represents the distance between cluster centroids i and j .

CHI measures the ratio of between-cluster dispersion to within-cluster dispersion:

$$CHI = \frac{Tr(Wk)}{Tr(Bk)} \times \frac{N - K}{K - 1} \quad (13)$$

Where $Tr(Wk)$ represents a trace of the between-cluster dispersion matrix; $Tr(Bk)$ is the trace of the within-cluster dispersion matrix; N represents the number of data points; K is the number of clusters.

2.5.2 Regression Modelling of PET

The modelling framework formulated both the mean of PET (PET_{mean}) and its standard deviation (PET_{std}) as functions of several remote sensing parameters:

$$PET_{mean} = f(T_{air_{ref}}, Solar_{ref}, V_{a_{ref}}, NDVI, MNDWI, NDBI, BSI, \alpha_{land}, \epsilon_{land}) \quad (14)$$

$$PET_{std} = f(T_{air_{ref}}, Solar_{ref}, V_{a_{ref}}, NDVI, MNDWI, NDBI, BSI, \alpha_{land}, \epsilon_{land}) \quad (15)$$

Where $T_{air_{ref}}$ is the reference dry-bulb air temperature; $Solar_{ref}$ is the reference global horizontal solar irradiance; $V_{a_{ref}}$ is the reference wind speed; $NDVI$ is the normalized difference vegetation index; $MNDWI$ is the modified normalized difference water index; $NDBI$ is the normalized difference built-up index; BSI is the bare soil index; $BAEI$ is the built-up area extraction index; α_{land} is the land surface albedo; ϵ_{land} is the land surface emissivity.

To predict these PET distribution characteristics, XGBoost (Chen et al., 2024) was employed with hyperparameters tuned across specific search spaces using Bayesian optimization from BayesSearchCV (Head et al., 2018), as shown in Table 3.

Table 3: Hyperparameter optimization range

Hyperparameter	Range
n_estimators	(50, 500)
learning_rate	(0.01, 0.3)
max_depth	(2, 10)
subsample	(0.5, 1.0)

Model performance was evaluated based on 5-fold cross-validation using Symmetric Mean Absolute Percentage Error (SMAPE), Root Mean Squared Error (RMSE) and the coefficient of determination (R^2). SMAPE penalizes the over-predictions and under-predictions symmetrically, suitable for actual values closing to zero, whereas RMSE penalizes larger errors in the residual squared process and is more interpretable in the same units as the original data.

$$SMAPE = \frac{100}{n} \sum_{i=1}^n \frac{2 \cdot |Y_i - \hat{Y}_i|}{|Y_i| + |\hat{Y}_i|} \quad (16)$$

$$RMSE = \sqrt{\frac{1}{n} \sum_{i=1}^n (Y_i - \hat{Y}_i)^2} \quad (17)$$

$$R^2 = 1 - \frac{\sum_{i=1}^n (Y_i - \hat{Y}_i)^2}{\sum_{i=1}^n (Y_i - \bar{Y})^2} \quad (18)$$

Where n represents the number of observations; Y_i denotes a given observation; \hat{Y}_i expresses the predicted value.

Model interpretation was conducted based on SHapley Additive exPlanations (SHAP) using shap Python package (Lundberg and Lee, 2017). SHAP quantifies the contribution of each input feature to individual model prediction, providing an interpretable link between predictors derived from satellite indices (e.g., $NDVI$, $NDBI$) and environmental variables (e.g., T_a , V_a) and the predicted mean and standard deviation of PET. The summary plot of SHAP provides the overall importance and effect

direction of key features, while dependence plots were created to illustrate the marginal effect of each feature on both mean and standard deviation of PET.

For PET inference, machine learning models were used to predict the PET_{mean} and PET_{std} based on reference meteorological data and remote sensing data at each grid point. Monte Carlo simulations with sampling size of 5000 were then implemented to draw repeated random samples from normal distribution determined by predicted PET_{mean} and PET_{std} .

3. Results

3.1 Clustering of Reference Weather Data

The optimal number of clusters was determined to be 3. As indicated in Figure 6 and Figure 5, the inertia score for 3 clusters was 17.33, indicating a significant reduction from the inertia score of 2 clusters, while remaining relatively lower compared to higher cluster numbers. The SC for 3 clusters was 0.38, which was the second highest value compared to other clustering results. The DBI and CHI for 3 clusters were 0.90 and 314.49, respectively, both of which were indicative of optimal clustering performance. These performance metrics suggested that 3 clusters provided a good balance between cluster separation and compactness for reference meteorological data.

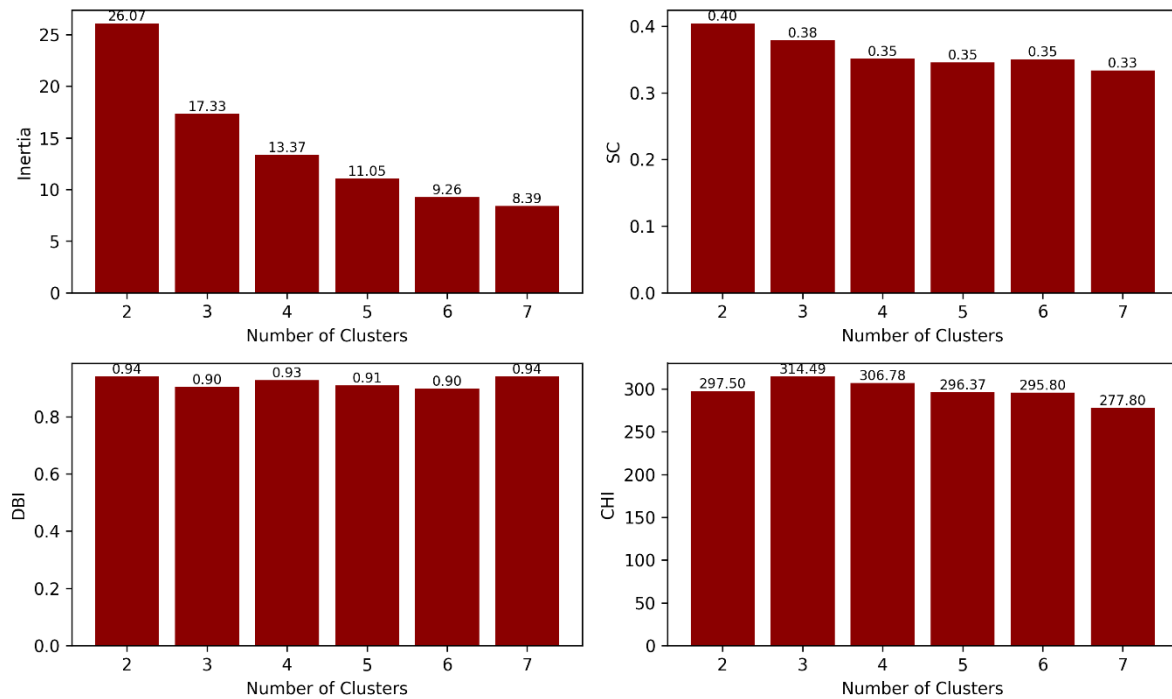


Figure 5: Clustering performance of reference weather data

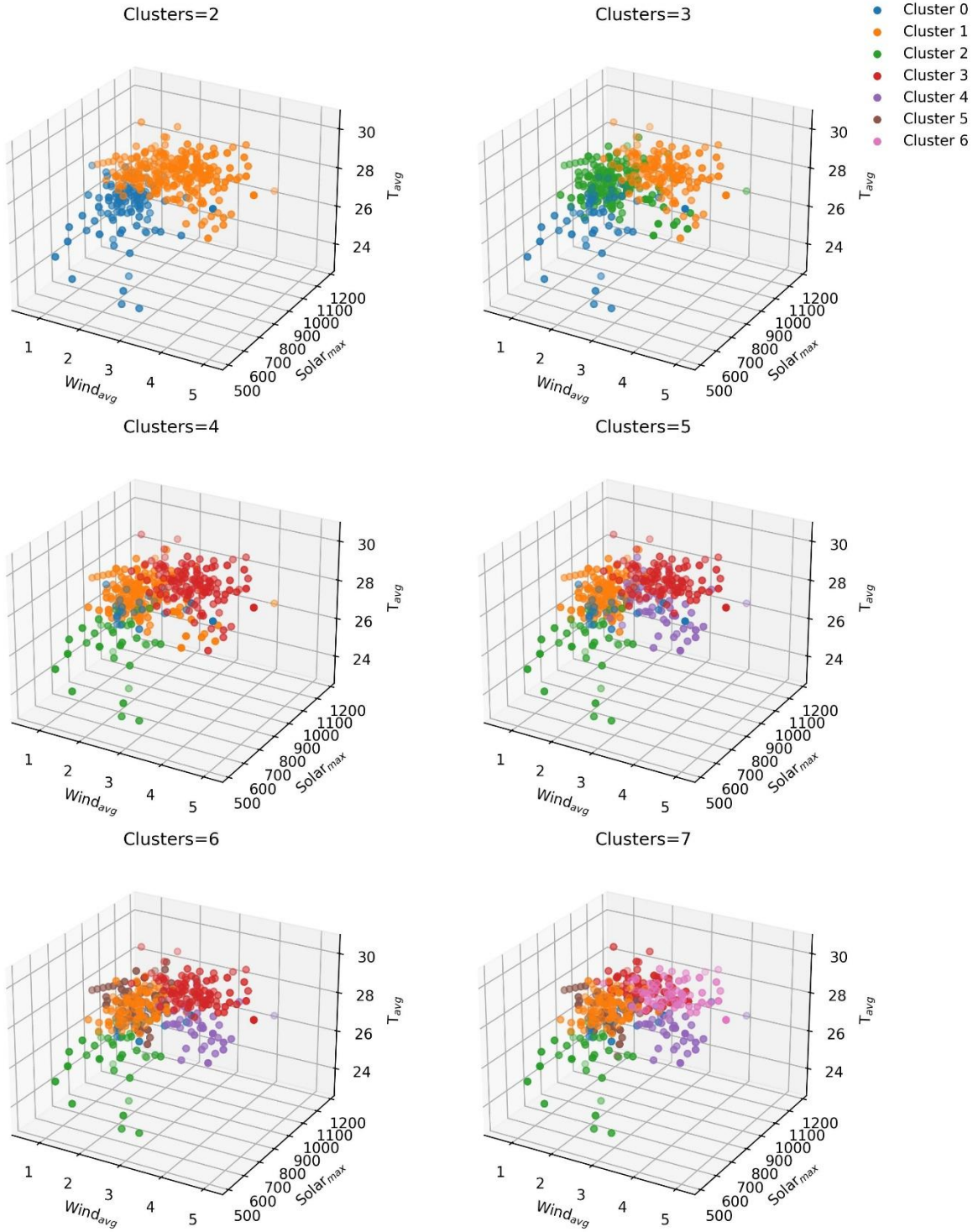


Figure 6: Clustering of reference weather data

The dates associated with Cluster 1 (Figure 6) of the optimal 3 clusters were extracted to filter out the representative local microclimate data. Table 4 summarises the descriptive statistics of this reference weather subset, signifying a clear, hot, and rain-free ($\text{Rain}_{\text{tot}} = 0 \text{ mm}$) weather condition. The daily mean of T_{avg} , T_{max} , T_{min} are 29.09°C , 32.25°C , 26.84°C , respectively. The daily $\text{Solar}_{\text{max}}$ was $838.86 \pm 58.99 \text{ W/m}^2$, and the daily Wind_{avg} was $3.27 \pm 0.61 \text{ m/s}$.

Table 4: Descriptive statistics of clustered weather data under clear and hot conditions

Statistic	Rain _{tot} (mm)	Wind _{avg} (m/s)	Solar _{tot} (W/m ²)	Solar _{max} (W/m ²)	Solar _{avg} (W/m ²)	T _{avg} (°C)	T _{max} (°C)	T _{min} (°C)
mean	0	3.27	7077.89	838.86	294.91	29.09	32.25	26.84
min	0	1.65	6117.5	740.4	254.9	27.26	30	25
25%	0	2.87	6695.45	798.1	278.98	28.67	32	26
50%	0	3.22	7017.4	825.15	292.39	29.1	32	27
75%	0	3.72	7424.75	877.4	309.36	29.51	33	27.5
max	0	4.72	8747.1	1014.6	364.46	30.42	34.5	28.9
std	0	0.61	569.13	58.99	23.71	0.62	0.9	0.85

3.2 Spatial and Temporal Heterogeneity of PET Across Sampled Locations

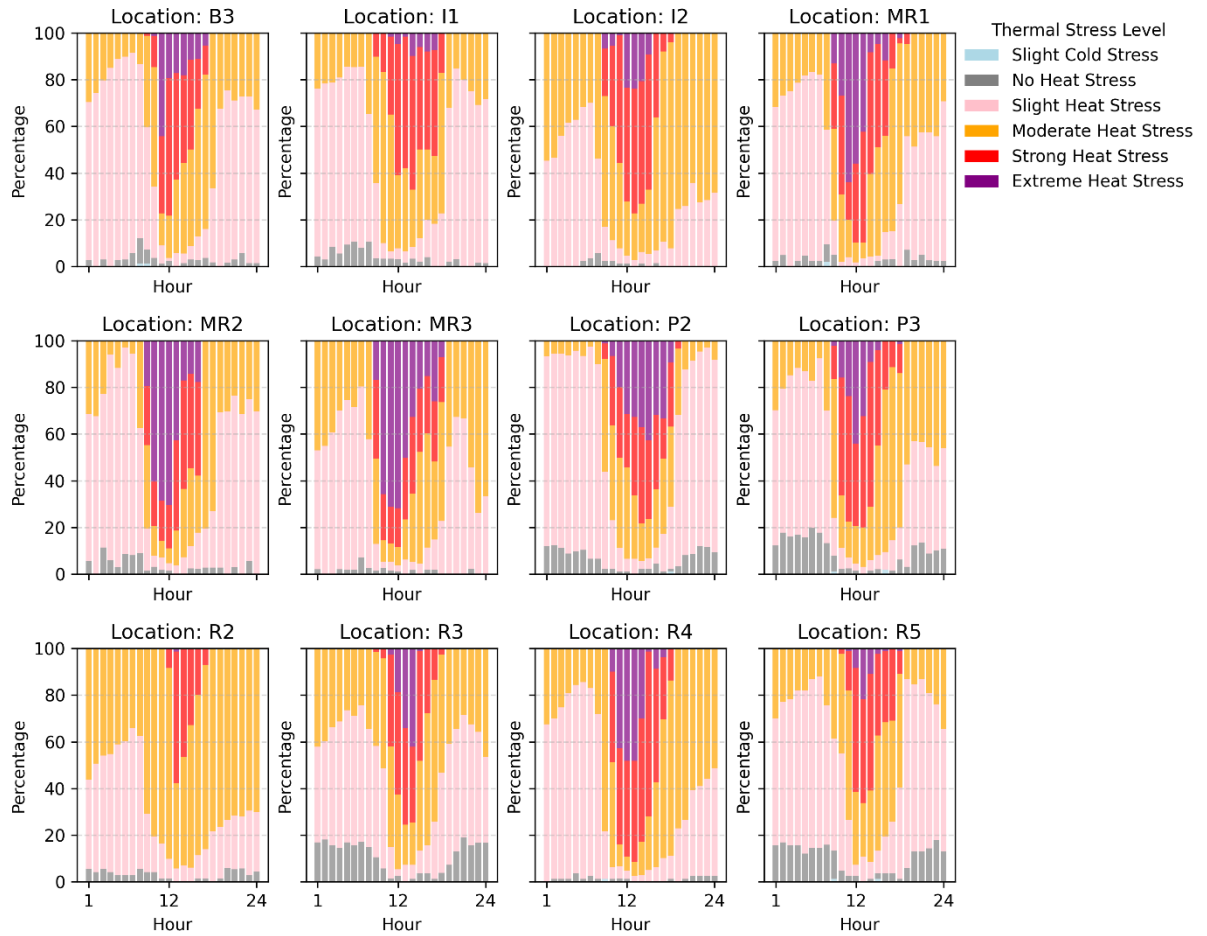


Figure 7: Spatial heterogeneity of PET across sampled locations

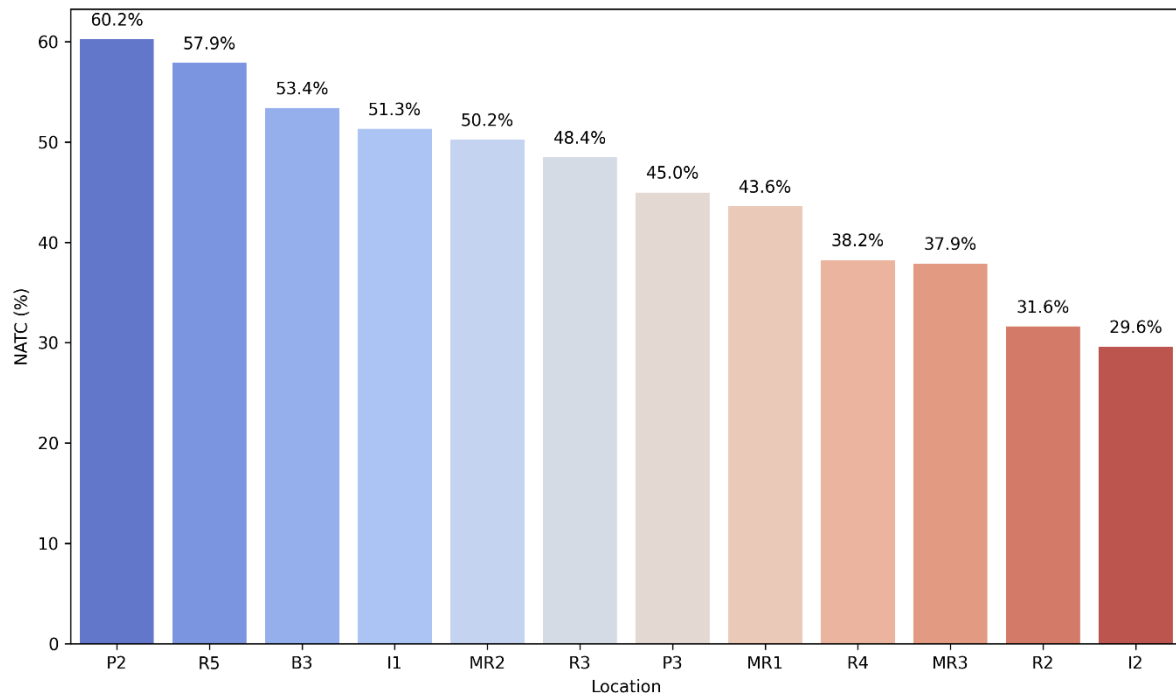


Figure 8: NATC across sampled locations

Thermal comfort varied significantly across different locations and times of the day with some locations experiencing more extreme conditions during specific hours (Figure 7). The thermal stress levels were categorized into five groups: slight cold stress, no heat stress, slight heat stress, moderate heat stress, strong heat stress, and extreme heat stress. As illustrated in Figure 8, the park site (P2) consistently exhibited high percentages of no heat stress and slight heat stress throughout the day, resulting in the highest NATC (60.2%). This can be attributed to the park's vegetative cover reducing land surface temperature and mean radiant temperature through shading and evapotranspiration. Another park site P3 (NATC= 45%) without dense tree canopy suggested a warmer environment in the evening. In the commercial district, B3 (53.4%), located centrally among buildings, maintained relatively high thermal acceptability, consistent with the shading effects of the surrounding urban canyon that mitigated peak radiant heat. Along major roads, MR2 (50.2%) adjacent to P2 showed relatively higher thermal comfort level. While MR1 (43.6%) and MR3 (37.9%), both situated near built-up areas, showed comparable NATC values with significant moderate heat stress indicating severe discomfort conditions due to its open roadway setting dominated by asphalt and lacking significant shading. Among residential sites, R5 (57.9%) exhibited mixed but generally acceptable thermal conditions, whereas R2 (31.6%) had the lowest overall acceptable thermal comfort and the highest percentage of moderate heat stress over 24 hours, indicating a persistent high temperature environment. I2 is located in an industrial area with a large low-rise building area and no greenery cover. It has the worst thermal comfort with a NATC of 29.6%.

The hourly heat stress analysis provides detailed information on when and where thermal comfort issues occurred. However, it required further analysis such as regression models to find out why certain locations exhibit different thermal comfort conditions under different urban morphologies, which is crucial for heat mitigation strategies to improve thermal comfort in specific locations and at specific times.

3.3 Probabilistic Prediction of PET

PET_{mean} was well-predicted by the optimized XGBoost model, achieving R^2 , RMSE and SMAPE of 0.93, 0.81 °C and 1.34%, respectively (Table 5). In contrast, the prediction of PET_{std} was more challenging with R^2 , RMSE and SMAPE reaching 0.85, 0.38 °C and 10.44%, respectively.

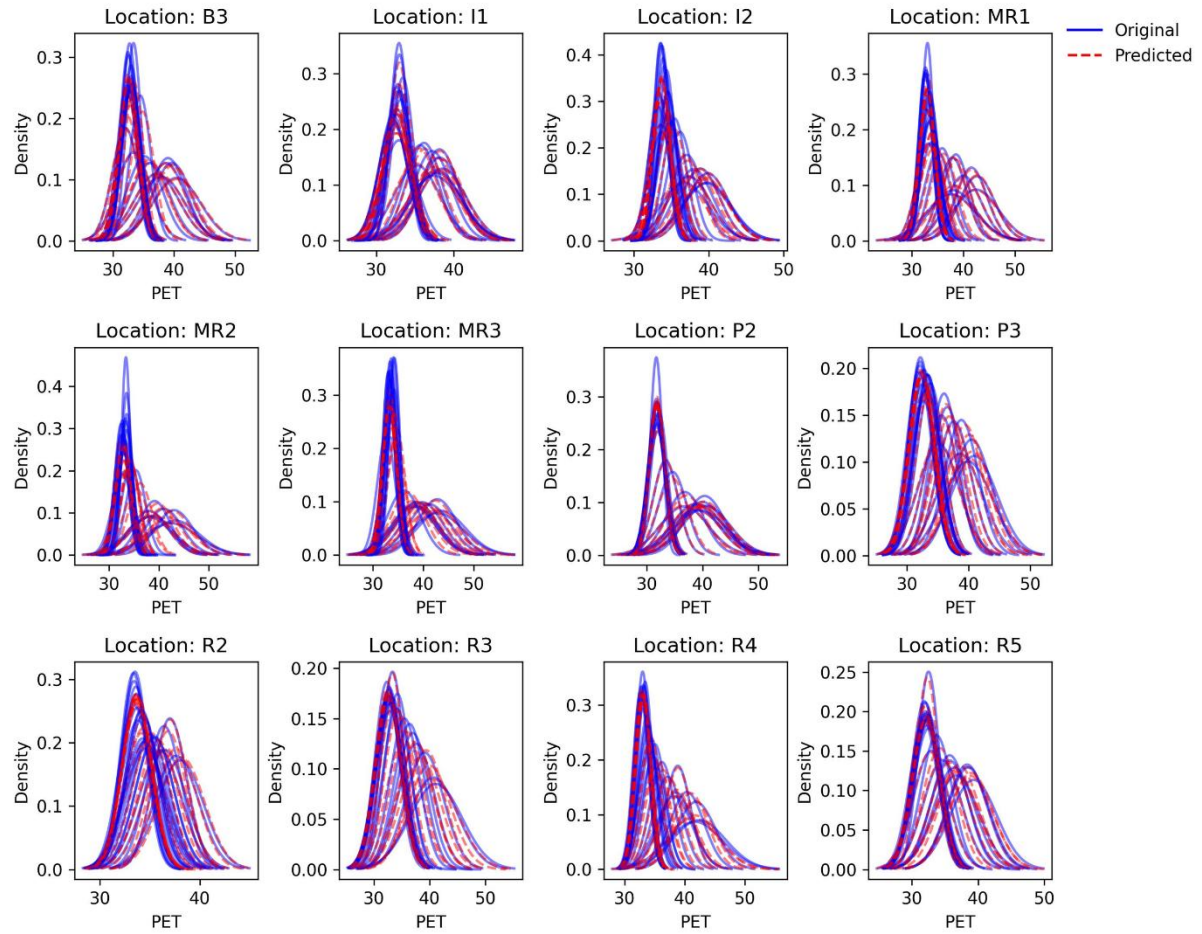
The distribution plots of PET_{mean} and PET_{std} at each location showed that the original values were in good agreement with the predicted values (Figure 9). The predicted values of some locations (e.g., B3, I1, I2, MR1-MR3, P2, and R2) were lower than the original peak values.

The residual analysis indicated that for PET_{mean} , most residuals were tightly clustered around 0 °C, with the majority falling within ± 2 °C and only a few observations exceeding 4 °C (Figure 9). The residuals were randomly distributed without temporal trends, although a slight underestimation was observed at higher PET values. For PET_{std} , residuals were narrower in absolute magnitude within ± 1 °C but exhibited a systematic pattern: higher observed variability tended to be underestimated, while lower variability was slightly overestimated, reflecting a regression-to-the-mean effect.

Table 5: Bayesian optimization results of hyperparameters and model performance of XGBoost

Target	learning_rate	max_depth	n_estimators	subsample	R^2	RMSE (°C)	SMAPE (%)
PET_{mean}	0.16	7	328	1	0.93	0.81	1.34
PET_{std}	0.06	9	273	0.92	0.85	0.38	10.44

a. PET distribution at different locations



b. Residual analysis of predicted PET

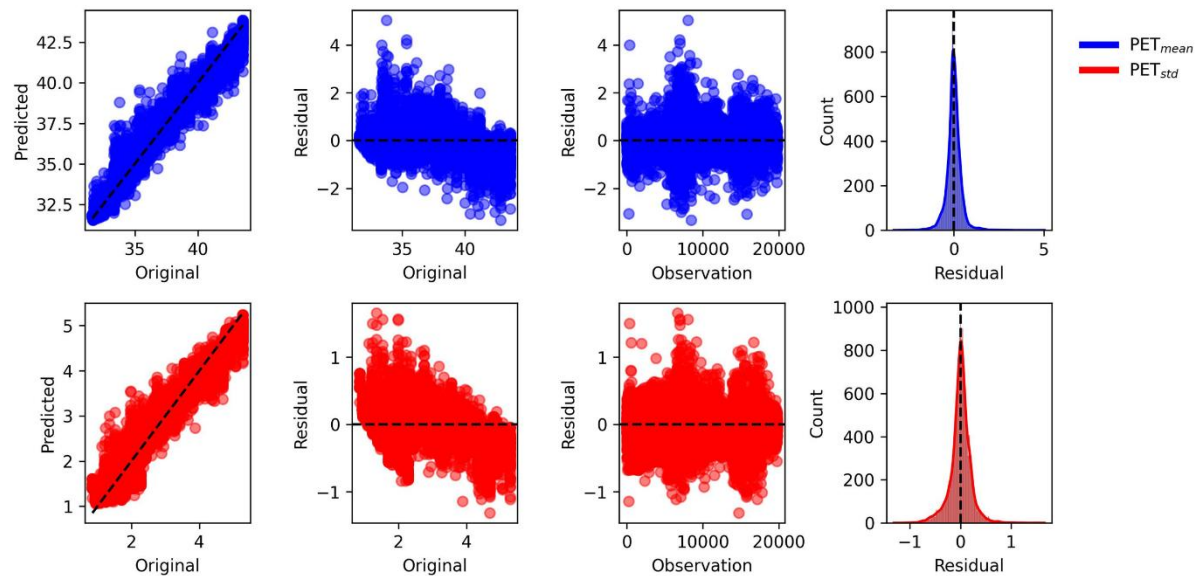
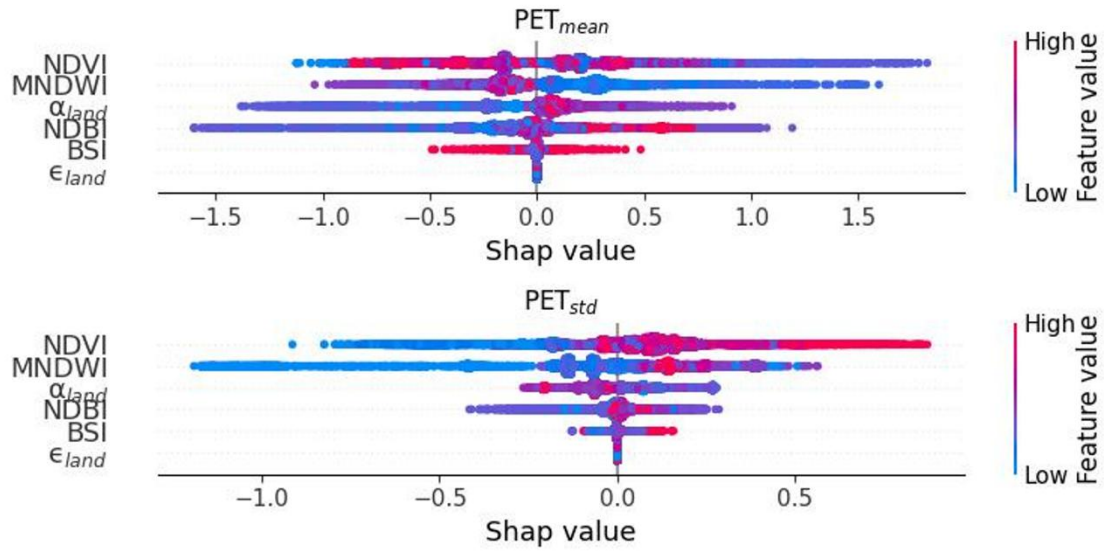


Figure 9: Evaluation of regression models: (a) Original and predicted PET distribution at different locations; (b) Residual analysis of mean and standard deviation of PET

Figure 10 presents the importance of input features and the partial dependence between various urban morphological features and their corresponding SHAP values for PET_{mean} and PET_{std} . The SHAP summary plot reveals that $NDVI$ was the most important urban morphological predictor, followed by $MNDWI$, α_{land} , $NDBI$, BSI and ϵ_{land} . For PET_{mean} , decreasing SHAP values were associated with increasing $MNDWI$ reflecting the well-established cooling influence of water bodies through evaporative advection. In contrast, the $NDBI$ displayed a positive relationship with increasing SHAP values. This reflects the urban heat island effect from built-up areas. $NDVI$ demonstrated a more complex and nonlinear relationship where both cooling and warming effects emerged. Lower $NDVI$ had a negative effect on PET_{mean} , whereas $NDVI > 0.2$ had a positive effect on PET_{mean} , indicating that the cooling potential of green spaces is related to the health of plants. α_{land} also exhibited a complex cooling potential but is generally negatively correlated with PET. In terms of PET_{std} , both $NDVI$ and $MNDWI$ were nonlinearly correlated with SHAP values indicating complex effects of vegetation cover and water bodies on thermal comfort variability. Meanwhile, the $NDBI$ was positively correlated with increasing SHAP values indicating that thermal comfort variance was higher in areas with higher built-up areas and bare soil. Regarding α_{land} , it consistently exerted a negative influence indicating that reflective surfaces reduced both mean heat load and short-term variability by lowering daytime heat gain. ϵ_{land} and BSI showed negligible influence for both PET_{mean} and PET_{std} .

a. Feature importance



b. Dependence analysis

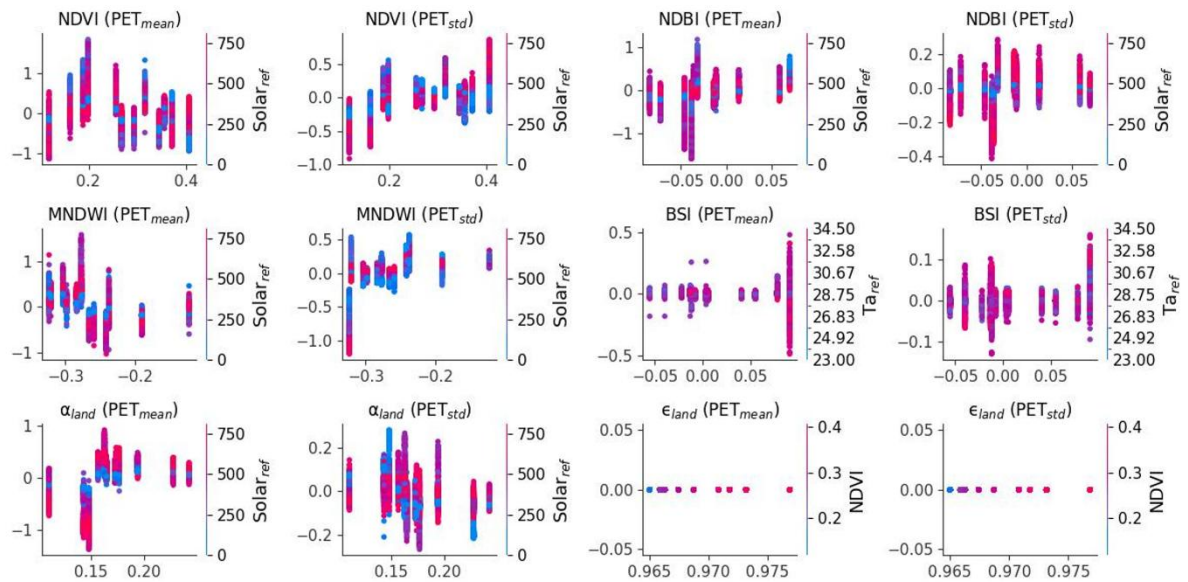


Figure 10: SHAP analysis of mean and standard deviation of PET: (a) Feature importance; (b) Dependence analysis

Outdoor thermal comfort assessments were conducted in the Jurong East area using trained models of PET_{mean} and PET_{std} . The prediction of NATC at Jurong East area (Figure 11) reveals a pronounced spatial heterogeneity in outdoor thermal comfort. Locations near to greenery cover, particularly areas with dense tree canopies and vegetated surfaces, achieve NATC up to 65%. In contrast, areas dominated by built-up surfaces, especially those with extensive impervious cover such as industrial or high-density residential areas, have NATC values below 30%. For PET_{mean} (Figure 12), the heatmap revealed a clear contrast between daytime (08:00–19:00) and nighttime (20:00–07:00) thermal conditions. The maximum PET_{mean} difference between hot and cold spots reached approximately 1.5 °C and 6 °C for nighttime and daytime, respectively. At night, cold spots were prominent in areas with dense greenery,

while hot spots were concentrated in heavily built-up zones, particularly industrial areas. During the day, areas with extensive tree canopy consistently exhibited the lowest PET, whereas some built-up areas also showed reduced PET due to self-shading effects. In terms of PET_{std} (Figure 13), greenery covered areas consistently showed lower thermal variability compared to built-up areas. During the daytime (08:00–19:00), thermal variability ranged from 4.0–4.5 °C in built-up areas and 1.5–2.0 °C in greenery covered areas. At night (20:00–07:00), the variability was reduced to 2.2–2.4 °C in built-up areas and 1.2–1.4 °C in greenery covered areas.

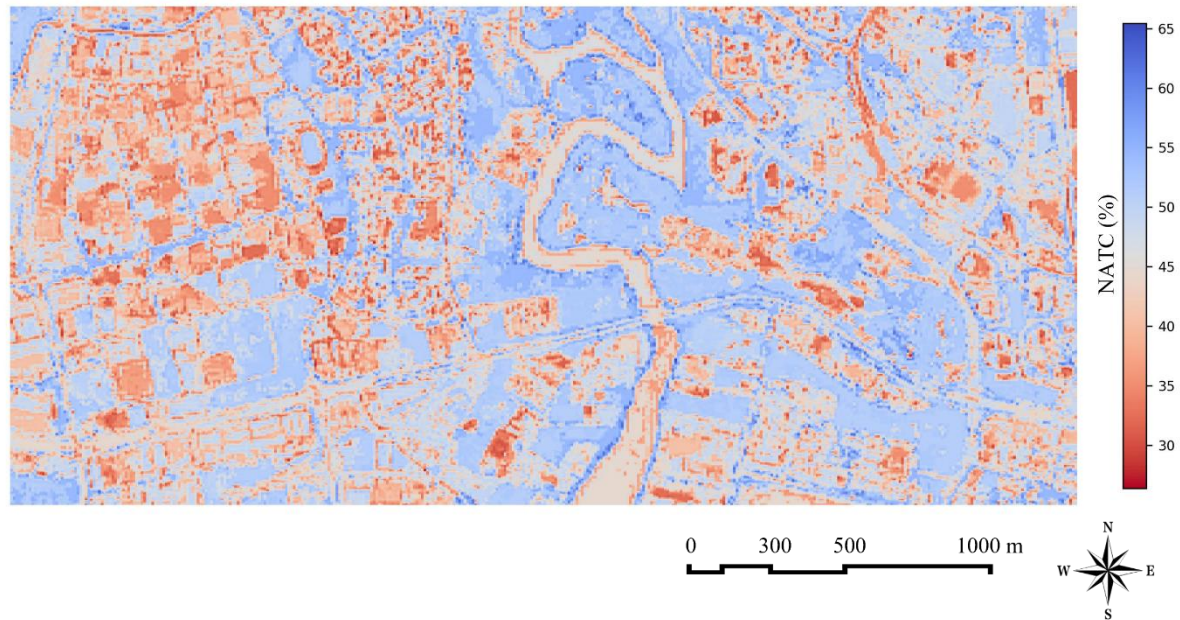


Figure 11: The prediction of NATC at Jurong East area

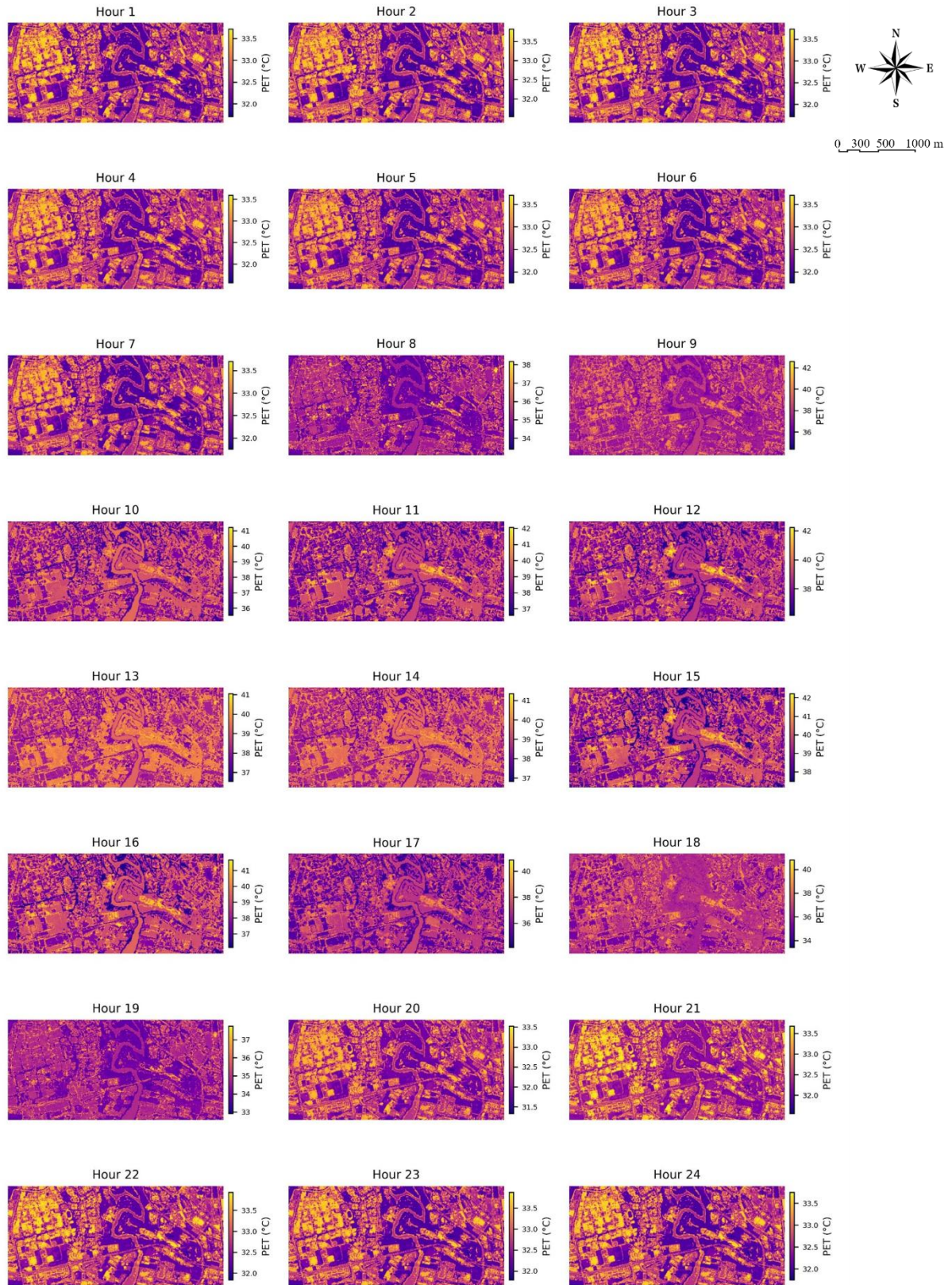


Figure 12: Hourly heatmap of PET_{mean} at Jurong East area

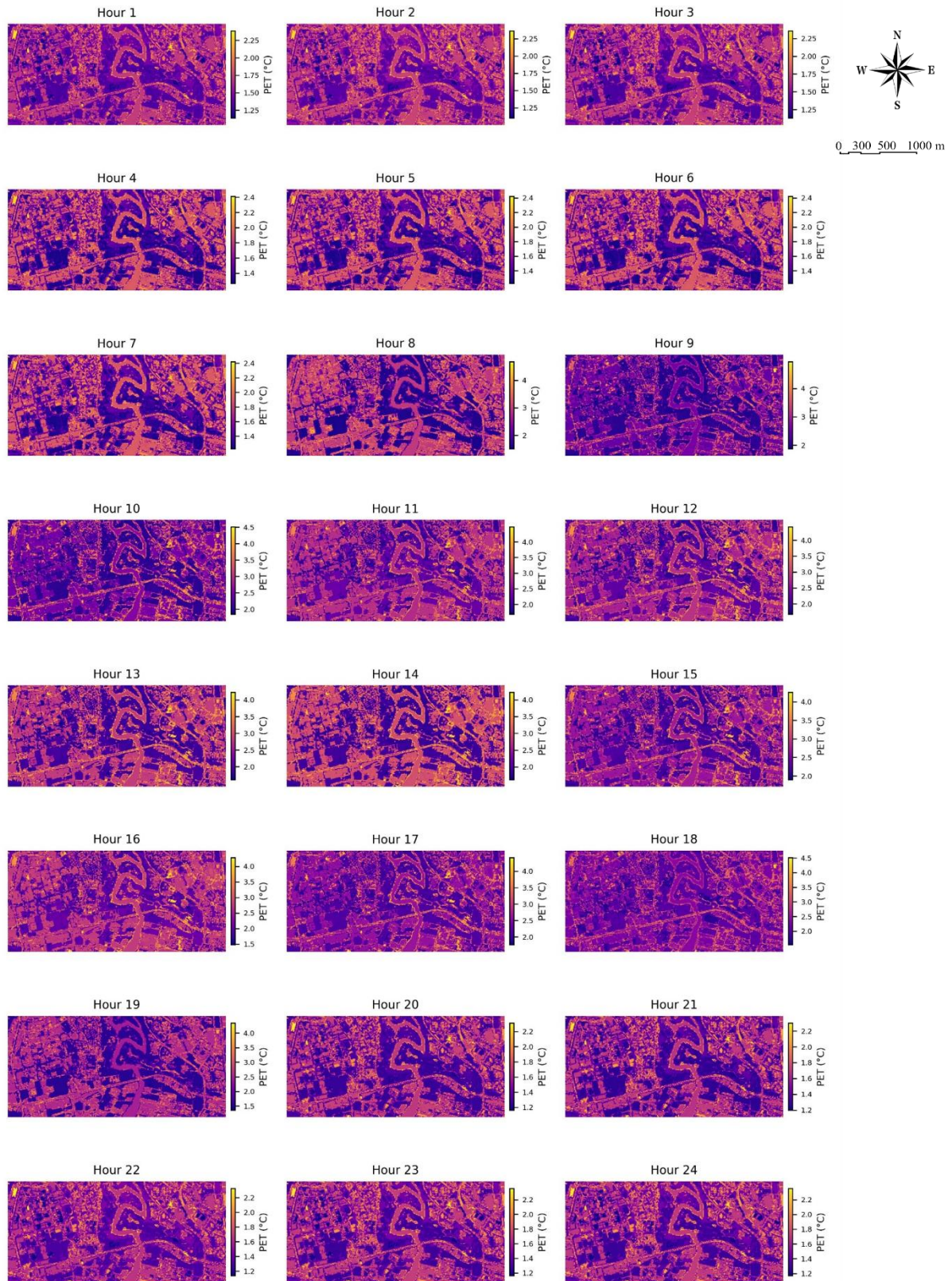


Figure 13: Hourly heatmap of PET_{std} at Jurong East area

4. Discussion

4.1 Stochastic representation of outdoor thermal comfort

As shown in Figure 8, the underlying distribution of PET over longer time periods exhibited substantial variability under clear, hot and rain-free weather conditions driven by both microclimatic fluctuations and interactions with urban morphologies. Previous studies based on short-term measurements (Elghezawy and Eltarabily, 2021; He et al., 2023; Miao et al., 2023; Ou and Lin, 2023; Sun et al., 2022; Tabatabaei and Fayaz, 2023; Zhao et al., 2023) often fail to capture the full range of thermal conditions. Furthermore, conventional regression modelling typically establish deterministic relations between a single thermal comfort index (e.g., PET, UTCI) and environmental or morphological indicators yielding average predictions but overlooking the temporal variability and probability of extreme stress levels (Anders et al., 2025; Deng et al., 2023; Jović et al., 2016; Pantavou et al., 2022; Young et al., 2022; Zhang et al., 2022).

In contrast, a stochastic approach explicitly represents thermal comfort as a distribution rather than a fixed value. By repeatedly sampling from the predicted PET distribution, stochastic simulations can capture the range of possible PET outcomes. This not only allows for an estimate of central tendency but also quantifies the uncertainty and risk associated with extreme heat stress. Since thermal comfort perception is probabilistic in nature caused by microclimate fluctuations, human metabolism, and individual clothing levels (Tartarini and Schiavon, 2020), it is essential to estimate both the expected conditions and the uncertainty around them. Human metabolism and personal clothing levels do not vary much within a given season. For example, people tend to walk and wear typical summer clothing during summer activities, therefore human metabolism and personal clothing levels were assigned to be 2 met and 0.5 clo in this study, respectively. In contrast, microclimate fluctuations strongly depend both on macroclimatic variations and on the surrounding urban morphologies. The latter is due to the fact that the urban morphologies have significant impacts on urban climate by altering the heat balance and wind characteristics within the urban canopy (Chen et al., 2020; Peng et al., 2022; Tong et al., 2017; Wu et al., 2022; Yu et al., 2020; Yuan et al., 2020), where a stochastic framework can provide a more realistic description of local variability and heat exposure.

The proposed framework advances urban thermal environment assessment by employing stochastic simulations characterizing heat stress events as a probabilistic distribution rather than single outcome. This approach not only quantifies average thermal comfort but also reveals the intensity and likelihood of extreme heat stress events that deterministic model tends to overlook. This enables more realistic assessments of heat exposure reflecting the heterogeneous microclimate dynamics within urban areas. It is also crucial for climate responsive design as adaptation strategies must address a range of plausible scenarios rather than optimizing for average conditions.

4.2 Key Drivers of Spatial and Temporal Thermal Stress

In terms of supervised machine learning, XGBoost proved effective for modelling nonlinear relationships between urban morphology and PET distributions achieving high predictive accuracy for PET_{mean} ($R^2 = 0.93$). This is expected as nonlinear relationships have been discovered between urban morphologies and local urban climatic variables such as T_a and T_{mrt} (Chen et al., 2023; Gu et al., 2024; Jia et al., 2024; Liu et al., 2024; Wu et al., 2022). Predictions of PET_{std} ($R^2 = 0.85$) were less precise underscoring the challenge of capturing fluctuations in thermal comfort. For the computation of urban morphological indicators, multispectral remote sensing data can provide continuous spatial assessment of urban morphology data with fine-resolution (e.g., 10 m) and efficient processing, which has been mainly used to estimate the land surface temperature (LST) as the two data have similar scales and resolutions (Chen et al., 2006; Jamei et al., 2022; Jia and Wang, 2020; Mangiameli et al., 2022). However, it is not sufficient to use only LST to estimate PET or UTCI, which requires T_a , T_{mrt} , RH, and V_a as environmental inputs. Therefore, ground-based microclimate measurements to capture the

change of T_a , T_{mrt} , RH, and V_a remain essential. Nonetheless, multispectral remote sensing data can help reduce reliance on 3D models, which are difficult to validate against the real world and often lack critical information such as building height at many sites. Combined with ground-based microclimate data, multispectral data represents a practical approach for estimating thermal comfort at the city scale.

This study identified $NDVI$, $MNDWI$, $NDBI$, and α_{land} as key drivers with significant importance in predicting outdoor thermal comfort. High albedo surfaces shift SHAP values into the negative range reflecting their ability to reflect a larger fraction of incident radiation and thus mitigate heat gain indicating a cooling influence (Lopez-Cabeza et al., 2022). Whereas low albedo surfaces produce positive SHAP values, signifying heat absorption and re-radiation from darker pavements and roofs. Higher $MNDWI$, indicative of proximity to open water, is associated with negative SHAP values due to evaporative cooling through advection from water bodies (Liu et al., 2024). Vegetation represented by $NDVI$ is generally expected to reduce PET through shading and evapotranspiration (Imran et al., 2021; Pérez et al., 2022). Higher $NDBI$ values correspond to positive SHAP contributions reflecting the thermal amplification from dense built-up surfaces. While the factors influencing PET_{mean} largely determine its absolute thermal conditions, the drivers of PET_{std} shape its temporal variability reflecting the magnitude of intra-period (e.g., diurnal) fluctuations in thermal comfort, underscoring the interplay between solar radiation, surface moisture, and land-cover characteristics in modulating the amplitude of thermal comfort variability in tropical urban environments.

In addition, this study revealed that both PET_{mean} and PET_{std} were lower in areas with healthy vegetation ($NDVI > 0.2$) and relatively limited building cover. Previous studies have demonstrated that greenery such as tree canopy plays a critical role by providing shade, moderating temperatures (e.g., T_{mrt} , T_a), and enhancing evapotranspiration, thereby helping to reduce heat exposure and improve thermal stability in urban outdoor environments (Chen et al., 2023; Imran et al., 2021; Jia et al., 2024; Pérez et al., 2022). This study shows greenery can not only mitigate the intensity of heat stress by lowering average thermal conditions, but also reduce the variation of heat stress across the space resulting in a more stable and comfortable microclimate.

4.3 Limitations and Future Studies

The proposed framework is applicable to any region and climate conditions, but requires the availability of ground-measured meteorological data and retrained machine learning models. Nevertheless, the study's reliance on data from a specific period and location in Singapore limits the generalizability of the findings. The 5-fold cross validation is based on random sampling of the dataset, and the remote sensing index is extracted with a buffer size of 100 m radius, therefore the model may perform differently under different random states and buffer sizes. Expanding the dataset to include longer time spans, more diverse locations and different buffer sizes would enhance the model's robustness and applicability. In addition, the use of remote sensing data introduces uncertainties related to data resolution, cloud cover, and calibration. Future work should explore higher-resolution satellite data and improved calibration techniques to enhance the reliability of input data. This would also involve validating the model against additional datasets from other regions to ensure its accuracy and generalizability.

5. Conclusions

Microclimatic conditions in the urban canopy are influenced by variable radiation fluxes and complex wind fields, causing significant spatiotemporal variability in thermal comfort. This variability, due to surface-atmosphere energy exchange, air turbulence, and shading, shall not be modeled using deterministic methods. This study established a probabilistic framework for predicting the spatial and temporal dimensions of outdoor thermal comfort intensity and its variability, uncovering the stochastic nature of thermal comfort in different urban morphologies. The main findings are as follows:

-
- The framework demonstrated strong predictive performance, with $R^2 = 0.93$, $RMSE = 0.81$ °C, and $SMAPE = 1.34\%$ for PET_{mean} , and $R^2 = 0.85$, $RMSE = 0.38$ °C, and $SMAPE = 10.44\%$ for PET_{std} . The key morphological drivers of spatial and temporal thermal stress were $NDVI$, $MNDWI$, $NDBI$, and α_{land} , with $NDVI$ being the dominated predictor.
 - Locations with healthy vegetation such as extensive tree canopy and turf cover, recorded NATC values as high as 65%. In contrast, locations dominated by impervious built-up surfaces such as industrial estates and high-density residential blocks showed NATC values below 30%.
 - Greenery plays a dual role in reducing the overall intensity of heat stress by lowering average thermal conditions and minimizing spatial variation in heat stress, thereby producing a more stable and comfortable microclimate. Specifically, daytime (08:00–19:00) PET variations ranged from 4.0–4.5 °C in built-up areas and 1.5–2.0 °C in vegetated areas, while nighttime (20:00–07:00) variations decreased to 2.2–2.4 °C in built-up areas and 1.2–1.4 °C in green cover areas.

Acknowledgements

This research was supported by: (1) The Fujian Province Young and Middle-aged Teacher Education and Research Project Funding (JAT241009); (2) Fuzhou University Research Starting Fund (511470); (3) Supporting Cooling NUS with Baseline-Evaluating-Action-Monitoring (BEAM) initiative from National University of Singapore.

Conflicts of Interest: The authors declare no conflict of interest.

References

- Anders, J., Schubert, S., Maronga, B., Salim, M., 2025. Simplifying heat stress assessment: Evaluating meteorological variables as single indicators of outdoor thermal comfort in urban environments. *Build. Environ.* 274, 112658.
- Arthur, D., Vassilvitskii, S., 2007. K-means++: The advantages of careful seeding. *Proc. Annu. ACM-SIAM Symp. Discret. Algorithms* 07-09-Janu, 1027–1035.
- ASHRAE, 2017. ANSI/ASHRAE Standard 55-2017: Thermal environmental conditions for human occupancy, ASHRAE Standard.
- Błażejczyk, K., Broede, P., Fiala, D., Havenith, G., Holmér, I., Jendritzky, G., Kampmann, B., Kunert, A., 2010. Principles of the new Universal Thermal Climate Index (UTCI) and its application to bioclimatic research in European scale. *Misc. Geogr. Reg. Stud. Dev.* 14, 91–102.
- Boeing, G., 2024. Modeling and Analyzing Urban Networks and Amenities with OSMnx 1–16.
- Bröde, P., Krüger, E.L., Rossi, F.A., Fiala, D., 2012. Predicting urban outdoor thermal comfort by the Universal Thermal Climate Index UTCI—a case study in Southern Brazil. *Int. J. Biometeorol.* 56, 471–480.
- Building and Construction Authority, 2021. Green Mark 2021 Technical Guide 1–36.
- Carlson, T., 2019. On the Relation between NDVI , Fractional Vegetation Cover , and Leaf Area Index 4257. [https://doi.org/10.1016/S0034-4257\(97\)00104-1](https://doi.org/10.1016/S0034-4257(97)00104-1)
- Chatterjee, U., Majumdar, S., 2022. Impact of land use change and rapid urbanization on urban heat island in Kolkata city: A remote sensing based perspective. *J. Urban Manag.* 11, 59–71. <https://doi.org/10.1016/j.jum.2021.09.002>
- Chen, H.C., Han, Q., de Vries, B., 2020. Urban morphology indicator analyzes for urban energy modeling. *Sustain. Cities Soc.* 52. <https://doi.org/10.1016/j.scs.2019.101863>
- Chen, S., Wong, N.H., Zhang, W., Ignatius, M., 2023. The impact of urban morphology on the spatiotemporal dimension of estate-level air temperature: A case study in the tropics. *Build. Environ.* 228, 109843. <https://doi.org/10.1016/j.buildenv.2022.109843>
- Chen, T., He, T., Benesty, M., 2024. XGBoost : eXtreme Gradient Boosting. *R Packag.* version 0.71-2 1–4.
- Chen, T., Meili, N., Fatichi, S., Hang, J., Tan, P.Y., Yuan, C., 2023. Effects of tree plantings with varying street aspect ratios on the thermal environment using a mechanistic urban canopy model. *Build. Environ.* 246. <https://doi.org/10.1016/j.buildenv.2023.111006>
- Chen, X.L., Zhao, H.M., Li, P.X., Yin, Z.Y., 2006. Remote sensing image-based analysis of the relationship between urban heat island and land use/cover changes. *Remote Sens. Environ.* 104, 133–146. <https://doi.org/10.1016/j.rse.2005.11.016>
- Deng, W., Xia, C., Chen, J., Jiang, Y., 2023. An Examination of the Thermal Comfort Impacts of *Ficus altissima* on the Climate in Lower Subtropical China during the Winter Season. *Sustain.* 15. <https://doi.org/10.3390/su15032427>

-
- Dobrovolný, P., Krahula, L., 2015. The spatial variability of air temperature and nocturnal urban heat island intensity in the city of Brno, Czech Republic. *Morav. Geogr. Reports* 23, 8–16. <https://doi.org/10.1515/mgr-2015-0013>
- Elgheznawy, D., Eltarabily, S., 2021. The impact of sun sail-shading strategy on the thermal comfort in school courtyards 202.
- Farhadi, H., Faizi, M., Sanaieian, H., 2019. Mitigating the urban heat island in a residential area in Tehran: Investigating the role of vegetation, materials, and orientation of buildings. *Sustain. Cities Soc.* 46. <https://doi.org/10.1016/j.scs.2019.101448>
- Fiala, D., Havenith, G., Bröde, P., Kampmann, B., Jendritzky, G., 2012. UTCI-Fiala multi-node model of human heat transfer and temperature regulation. *Int. J. Biometeorol.* 56, 429–441.
- Fiorillo, E., Brilli, L., Carotenuto, F., Cremonini, L., Gioli, B., Giordano, T., Nardino, M., 2023. Diurnal Outdoor Thermal Comfort Mapping through Envi-Met Simulations, Remotely Sensed and In Situ Measurements. *Atmosphere (Basel)*. 14. <https://doi.org/10.3390/atmos14040641>
- Gorelick, N., Hancher, M., Dixon, M., Ilyushchenko, S., Thau, D., Moore, R., 2017. Google Earth Engine: Planetary-scale geospatial analysis for everyone. *Remote Sens. Environ.* 202, 18–27.
- Gu, X., Wu, Z., Liu, X., Qiao, R., Jiang, Q., 2024. Exploring the Nonlinear Interplay between Urban Morphology and Nighttime Thermal Environment. *Sustain. Cities Soc.* 101. <https://doi.org/10.1016/j.scs.2024.105176>
- Guo, A., Yue, W., Yang, J., He, T., Zhang, M., Li, M., 2022. Divergent impact of urban 2D/3D morphology on thermal environment along urban gradients. *Urban Clim.* 45. <https://doi.org/10.1016/j.uclim.2022.101278>
- He, X., Gao, W., Wang, R., Yan, D., 2023. Study on outdoor thermal comfort of factory areas during winter in hot summer and cold winter zone of China 228.
- He, Y., Liang, C., Liu, J., Dai, M., Cui, H., Chen, S., Lu, J., Li, Z., Li, C., 2025. An experimental and modeling study of thermal behavior of photovoltaic-greenery system. *Sustain. Cities Soc.* 126.
- Head, T., Louppe, G., Shcherbatyi, I., Vin\`icius, Z., Schröder, C., Campos, N., Young, T., Cereda, S., Fan, T., Shi, K., others, 2018. scikit-optimize/scikit-optimize: v0. 5.2. Zenodo.
- Höppe, P., 1999. The physiological equivalent temperature - a universal index for the biometeorological assessment of the thermal environment. *Int. J. Biometeorol.* 43, 71–75.
- Hwang, J., Jeong, Jaewook, Lee, M., Jeong, Jaemin, Lee, J., 2023. Establishment of outdoor thermal comfort index groups for quantifying climate impact on construction accidents. *Sustain. Cities Soc.* 91. <https://doi.org/10.1016/j.scs.2023.104431>
- Imran, H.M., Hossain, A., Islam, A.K.M.S., Rahman, A., Bhuiyan, M.A.E., Paul, S., Alam, A., 2021. Impact of Land Cover Changes on Land Surface Temperature and Human Thermal Comfort in Dhaka City of Bangladesh. *Earth Syst. Environ.* 5, 667–693. <https://doi.org/10.1007/s41748-021-00243-4>
- Jamei, Y., Seyedmahmoudian, M., Jamei, E., Horan, B., Mekhilef, S., Stojcevski, A., 2022. Investigating the Relationship between Land Use/Land Cover Change and Land Surface Temperature Using Google Earth Engine; Case Study: Melbourne, Australia. *Sustain.* 14. <https://doi.org/10.3390/su142214868>

-
- Jia, S., Wang, Y., 2020. Effects of land use and land cover pattern on urban temperature variations: A case study in Hong Kong. *Urban Clim.* 34, 100693. <https://doi.org/10.1016/j.uclim.2020.100693>
- Jia, S., Wang, Y., Hien Wong, N., Liang Tan, C., Chen, S., Weng, Q., Ming Mak, C., 2024. Estimation of mean radiant temperature across diverse outdoor spaces: A comparative study of different modeling approaches. *Energy Build.* 310, 114068. <https://doi.org/10.1016/j.enbuild.2024.114068>
- Jović, S., Arsić, N., Vilimonović, J., Petković, D., 2016. Thermal sensation prediction by soft computing methodology. *J. Therm. Biol.* <https://doi.org/10.1016/j.jtherbio.2016.07.005>
- Kumar Gavskeer, K., 2023. Urban growth, changing relationship between biophysical factors and surface thermal characteristics: A geospatial analysis of Agra city, India. *Sustain. Cities Soc.* 94, 104542. <https://doi.org/10.1016/j.scs.2023.104542>
- Lamberti, G., Boggetti, R., Kämpf, J.H., Fantozzi, F., Leccese, F., Salvadori, G., 2023. Development and comparison of adaptive data-driven models for thermal comfort assessment and control. *Total Environ. Res. Themes* 8. <https://doi.org/10.1016/j.totert.2023.100083>
- Li, Y., Gao, F., Yu, J., Fei, T., 2025. Machine learning based thermal comfort prediction in office spaces: Integrating SMOTE and SHAP methods. *Energy Build.* 329, 115267. <https://doi.org/10.1016/j.enbuild.2024.115267>
- Lillesand, T., Kiefer, R.W., Chipman, J., 2015. Remote sensing and image interpretation. John Wiley & Sons.
- Lim, T.K., Wong, N.H., Ignatius, M., Martin, M., Juang, H.M.H., Lou, J., Tiong, R.L.K., 2021. Singapore: An Integrated Multi-scale Urban Microclimate Model for Urban Planning in Singapore. *Biometeorology* 5, 189–217. https://doi.org/10.1007/978-3-030-87598-5_9
- Liu, X., Liu, Z., Zhu, Z., Qiao, R., 2024. Decoupling the multi-drivers of urban extreme heat environment in urban agglomerations using ensemble learning. *Build. Environ.* 258. <https://doi.org/10.1016/j.buildenv.2024.111618>
- Lopez-Cabeza, V.P., Alzate-Gaviria, S., Diz-Mellado, E., Rivera-Gomez, C., Galan-Marin, C., 2022. Albedo influence on the microclimate and thermal comfort of courtyards under Mediterranean hot summer climate conditions. *Sustain. Cities Soc.* 81, 103872. <https://doi.org/10.1016/j.scs.2022.103872>
- Lundberg, S.M., Lee, S.-I., 2017. A Unified Approach to Interpreting Model Predictions, in: Guyon, I., Luxburg, U. V, Bengio, S., Wallach, H., Fergus, R., Vishwanathan, S., Garnett, R. (Eds.), *Advances in Neural Information Processing Systems* 30. Curran Associates, Inc., pp. 4765–4774.
- Mangiameli, M., Mussumeci, G., Gagliano, A., 2022. Evaluation of the Urban Microclimate in Catania using Multispectral Remote Sensing and GIS Technology. *Climate* 10. <https://doi.org/10.3390/cli10020018>
- Miao, C., He, X., Gao, Z., Chen, W., He, B., 2023. Assessing the vertical synergies between outdoor thermal comfort and air quality in an urban street canyon based on field measurements 227.
- Muniz-Gaal, L.P., Pezzuto, C.C., Carvalho, M.F.H. de, Mota, L.T.M., 2020. Urban geometry and the microclimate of street canyons in tropical climate. *Build. Environ.* 169. <https://doi.org/10.1016/j.buildenv.2019.106547>

-
- Musco, F., Appiotti, F., Bianchi, I., Fontana, M.D., Gissi, E., Lucertini, G., Magni, F., Maragno, D., 2016. Planning and climate change: Concepts, approaches, design. Counteracting Urban Heat Isl. Eff. a Glob. Clim. Chang. Scenar. xxxvii–xlvi. <https://doi.org/10.1007/978-3-319-10425-6>
- Mzid, N., Pignatti, S., Huang, W., Casa, R., 2021. An analysis of bare soil occurrence in arable croplands for remote sensing topsoil applications. *Remote Sens.* 13, 1–24. <https://doi.org/10.3390/rs13030474>
- Ou, H., Lin, T., 2023. Effects of orientation and dimensions of shading structures on thermal comfort 243.
- Pantavou, K., Delibasis, K.K., Nikolopoulos, G.K., 2022. Machine learning and features for the prediction of thermal sensation and comfort using data from field surveys in Cyprus. *Int. J. Biometeorol.* 66, 1973–1984. <https://doi.org/10.1007/s00484-022-02333-y>
- Pedregosa, F., Varoquaux, G., Gramfort, A., Michel, V., Thirion, B., Grisel, O., Blondel, M., Prettenhofer, P., Weiss, R., Dubourg, V., Vanderplas, J., Passos, A., Cournapeau, D., Brucher, M., Perrot, M., Duchesnay, É., 2011. Scikit-learn: Machine learning in Python. *J. Mach. Learn. Res.*
- Peng, W., Wang, R., Duan, J., Gao, W., Fan, Z., 2022. Surface and canopy urban heat islands: Does urban morphology result in the spatiotemporal differences? *Urban Clim.* 42. <https://doi.org/10.1016/j.uclim.2022.101136>
- Pérez, G., Coma, J., Chàfer, M., Cabeza, L.F., 2022. Seasonal influence of leaf area index (LAI) on the energy performance of a green facade. *Build. Environ.* 207. <https://doi.org/10.1016/j.buildenv.2021.108497>
- Rikimaru, A., Roy, P.S., Miyatake, S., 2002. Tropical forest cover density mapping. *Trop. Ecol.* 43, 39–47.
- Smith, R.B., 2010. The heat budget of the earth ' s surface deduced from space (R . B . Smith ; Version : March , 2010) 2 . Solar Radiation (VIS and SWIR) a . Basic equations. *Terrain* 1–10.
- Sobrino, J.A., Jiménez-Muñoz, J.C., Paolini, L., 2004. Land surface temperature retrieval from LANDSAT TM 5. *Remote Sens. Environ.* 90, 434–440.
- Sobrino, J.A., Jiménez-muñoz, J.C., Sòria, G., Romaguera, M., Guanter, L., Moreno, J., Member, A., Plaza, A., Member, S., Martínez, P., 2008. Land Surface Emissivity Retrieval From Different VNIR and TIR Sensors 46, 316–327.
- Spagnolo, J., De Dear, R., 2003. A field study of thermal comfort in outdoor and semi-outdoor environments in subtropical Sydney Australia. *Build. Environ.* 38, 721–738.
- Sun, C., Lian, W., Liu, L., Dong, Q., Han, Y., 2022. The impact of street geometry on outdoor thermal comfort within three different urban forms in severe cold region of China 222.
- Tabatabaei, S.S., Fayaz, R., 2023. The effect of facade materials and coatings on urban heat island mitigation and outdoor thermal comfort in hot semi-arid climate 243.
- Tan, C.L., Wong, N.H., Jusuf, S.K., 2013. Outdoor mean radiant temperature estimation in the tropical urban environment. *Build. Environ.* 64, 118–129. <https://doi.org/10.1016/j.buildenv.2013.03.012>
- Tartarini, F., Schiavon, S., 2020. pythermalcomfort: A Python package for thermal comfort research. *SoftwareX* 12, 100578. <https://doi.org/10.1016/j.softx.2020.100578>

-
- Tong, S., Hien, N., Liang, C., Kardinal, S., Ignatius, M., Tan, E., 2017. Impact of urban morphology on microclimate and thermal comfort in northern China 155, 212–223.
- Valor, E., Caselles, V., 1996. Mapping Land Surface Emissivity from NDVI : Application to European , African , and South American Areas 184, 167–184.
- Vuckovic, M., Kiesel, K., Mahdavi, A., 2016. Toward advanced representations of the urban microclimate in building performance simulation 27, 356–366.
- Walther, E., Goestchel, Q., 2018. The P.E.T. comfort index: Questioning the model. *Build. Environ.* 137, 1–10. <https://doi.org/10.1016/j.buildenv.2018.03.054>
- Wu, Z., Qiao, R., Zhao, S., Liu, X., Gao, S., Liu, Z., Ao, X., Zhou, S., Wang, Z., Jiang, Q., 2022. Nonlinear forces in urban thermal environment using Bayesian optimization-based ensemble learning. *Sci. Total Environ.* 838. <https://doi.org/10.1016/j.scitotenv.2022.156348>
- Xu, H., 2006. Modification of normalised difference water index (NDWI) to enhance open water features in remotely sensed imagery. *Int. J. Remote Sens.* 27, 3025–3033. <https://doi.org/10.1080/01431160600589179>
- Young, E., Kastner, P., Dogan, T., Chokhachian, A., Mokhtar, S., Reinhart, C., 2022. Modeling outdoor thermal comfort along cycling routes at varying levels of physical accuracy to predict bike ridership in Cambridge, MA. *Build. Environ.* 208, 108577. <https://doi.org/10.1016/j.buildenv.2021.108577>
- Yu, Z., Chen, S., Wong, N.H., 2020. Temporal variation in the impact of urban morphology on outdoor air temperature in the tropics: A campus case study. *Build. Environ.* 181. <https://doi.org/10.1016/j.buildenv.2020.107132>
- Yuan, C., Sukma, A., Mei, S., He, W., Li, X., Norford, L., 2020. Mitigating intensity of urban heat island by better understanding on urban morphology and anthropogenic heat dispersion 176.
- Zha, Y., Gao, J., Ni, S., 2003. Use of normalized difference built-up index in automatically mapping urban areas from TM imagery. *Int. J. Remote Sens.* 24, 583–594. <https://doi.org/10.1080/01431160304987>
- Zhang, X., Yang, L., Luo, R., Wu, H.-Y., Xu, J., Huang, C., Ruan, Y., Zheng, X., Yao, J., 2022. Estimating the outdoor environment of workers’ villages in East China using machine learning. *Build. Environ.* 226, 109738.
- Zhao, J., Dong, J., Zhang, X., Na, Y., Jiang, C., 2023. Field measurement of microclimate of sunken square and its effect on indoor environment of underground metro station in subtropical region 228.